RSC Advances

PAPER

View Article Online
View Journal | View Issue

Cite this: *RSC Adv.*, 2025, **15**, 44173

Structure guided design and molecular modelling of a novel peptide–SWCNT biosensor targeting NS1 dengue virus

Putri Hawa Syaifie,[a] Sherlyna Anugerah Putri,[b] Farisa Aliya,[b] Muhammad Miftah Jauhar,[a] Muhammad Faozi Rahman Wakhid,[a] Etik Mardliyati,[c] Rikson Siburian,[de] Yudan Whulanza[f] and Isa Anshori *[b]

Reliable detection of the dengue virus nonstructural protein 1 (NS1) is critical for early diagnosis of serotype 2 (DENV-2) infections, especially in endemic regions such as Indonesia. Here, we report a fully *in silico* framework for the rational design and evaluation of a peptide–single wall carbon nanotube (SWCNT) biosensor interface targeting NS1 DENV-2. Starting from phylogenetic selection of a conserved Indonesian NS1 sequence, we combined homology modeling, advanced protein and peptide modelling to generate an initial biorecognition element, which was then optimized *via* point mutations predicted by binding free energy analysis. Of 13 candidates, a single variant (Mut-11) exhibited the most favorable docking score and lowest predicted ΔG, and maintained key hydrogen-bond interactions and minimal root-mean-square deviation (RMSD) during 25 ns molecular dynamics simulations. Dynamic simulations revealed structural changes indicating that this peptide binds selectively to dengue viruses, while showing limited interaction with zika virus. To assess sensor integration, Mut-11 was conjugated virtually to SWCNT surfaces using a pyrene-based linker. Simulations confirmed stable π–π stacking without disrupting SWCNT electronic integrity or peptide conformation. While this study provides a comprehensive computational framework for peptide-based nanobiosensor design, it is limited by the absence of experimental validation. Future *in vitro* studies, such as binding assays and biosensor prototype testing, are essential to confirm the predicted binding affinities and sensor performance, thereby bridging the gap between computational modeling and real-world application.

Received 5th July 2025
Accepted 6th November 2025

DOI: 10.1039/d5ra04799d

rsc.li/rsc-advances

1. Introduction

Dengue disease is mainly caused by the bites of *Aedes aegypti* and *Aedes albopictus* mosquitoes, which carry the dengue virus (DENV), leading to an acute viral infectious disease.[1,2] DENV has four serotypes: DENV-1, DENV-2, DENV-3, and DENV-4.[3,4] With rising global temperatures and population mobility, dengue infection cases are increasing significantly due to the rapid transmission and lack of effective treatment.[5] In 2021, dengue had a global age-standardized incidence rate (ASIR) of 752.04 cases per 100 000 population (95% uncertainty interval [UI]: 196.33–1363.35), resulting in an estimated 58.96 million cases worldwide. The global age-standardized mortality rate (ASMR) was 0.38 deaths per 100 000 population (95% UI: 0.23–0.51), corresponding to approximately 29 077 deaths. That year, Indonesia recorded the highest ASMR at 4.24 per 100 000 population (95% UI: 2.58–6.05), while India reported the highest number of dengue-related deaths, with an estimated 14 282 fatalities (95% UI: 7630–21,082).[2] Hence, dengue has already become a great threat to global public health recently.

The most common outbreak-causing serotypes are DENV-1 and DENV-2.[6,7] Additionally, DENV-2 and DENV-4 are known to cause severe illness, such as dengue hemorrhagic fever (DHF), whereas DENV-1 and DENV-3 typically result in milder symptoms or may even go unnoticed.[8] Studies have shown that outbreaks of DENV-2 are linked to the highest overall mortality rates. Research has also demonstrated that DENV-2 tends to cause more severe secondary infections compared to other serotypes, resulting in the worst manifestation of the disease.[9–11] In the dengue case in Indonesia, DENV-2 has been the most prevalent serotype contributing to the dengue

[a]*Center of Excellence Life Sciences, Nano Center Indonesia, South Tangerang, 15314, Indonesia*

[b]*Lab on Chip Laboratory, Biomedical Engineering Department, School of Electrical Engineering and Informatics, Institut Teknologi Bandung, Bandung, 40132, Indonesia. E-mail: isaa@staff.stei.itb.ac.id*

[c]*Research Center for Nanotechnology System, National Research and Innovation Agency (BRIN), Tangerang Selatan, 15314, Indonesia*

[d]*Department of Chemistry, Faculty of Mathematics and Natural Sciences, Universitas Sumatera Utara, Medan 20155, Indonesia*

[e]*Carbon and Frankincense Research Center-Universitas Sumatera Utara, Medan 20155, Indonesia*

[f]*Department of Mechanical Engineering, University of Indonesia, Depok, 16424, Indonesia*

outbreak in recent years.[12] These findings highlight the significant role of DENV-2 in shaping dengue epidemiology and its contribution to the global health burden.

As there is currently no specific treatment or vaccine to mitigate the impact of dengue, early detection and accurate diagnostics are essential for effective disease management.[13] Traditionally, diagnostic approaches such as hemagglutination inhibition (HI) assays, PCR, ELISA, plaque reduction neutralization tests (PRNT), and virus isolation are widely used in laboratories, and the direct isolation of the virus is the gold standard.[13] However, these conventional methods are often expensive, time-consuming. Moreover, there is a remaining challenge regarding the specificity of the detection methods, as false positives may occur in those with infection by other flaviviruses (Japanese Encephalitis virus (JEV), yellow fever virus (YFV), or zika virus (ZIKV)).[13]

The nonstructural 1 (NS1) antigen plays a crucial role in the replication of dengue virus (DENV) within host cells and is released into the bloodstream of infected individuals, making it a key early-stage biomarker for detecting flavivirus infections.[14–16] In clinical practice, serum NS1 levels usually range from 0.04 to 2 μg mL^{-1} in patients experiencing a primary dengue infection, and from 0.01 to 2 μg mL^{-1} in those with secondary infections. NS1 is particularly useful for diagnosing dengue in its acute phase, as it stays detectable in the bloodstream longer than the virus itself.[17] However, as stated before, the sensitivity of the diagnostic instruments remains a challenge, the existing NS1 diagnostic product approved by the FDA only has the best sensitivity for DENV-1.[8] In Indonesia, the sensitivity detection of NS1 for DENV-2 using existing methods is only around 68.4%.[18] Therefore, we are eager to develop a more sensitive approach for NS1 DENV-2 detection, especially for the virus strain in Indonesia.

Linear and uniquely structured small peptides are gaining popularity as effective affinity reagents in the development of next-generation biosensors. Small peptides are increasingly recognized as promising candidates for the development of biorecognition elements (BREs) due to their ease of synthesis, low cost, environmental stability, and low molecular weight. Additionally, a wide range of peptide sources can be utilized to create effective BREs, as they can interact with diverse surfaces or be functionalized to form specific, stable, and efficient biosensor complexes.[19,20]

Recent advancements in biosensor technologies have highlighted the potential of peptide-functionalized carbon nanotubes (CNTs) as effective platforms for virus detection. Among various carbon-based nanomaterials, single-walled carbon nanotubes (SWCNTs) have emerged as highly promising due to their exceptional electrical conductivity, high current mobility, thermal stability, and nanoscale diameter.

Peptide-CNT thin-film transistors (TFTs) have demonstrated sequence-independent nucleic acid detection through electrostatic interactions. For instance, a decapeptide functionalized with pyrene groups was shown to adsorb onto CNTs *via* π–π stacking, enabling sensitive RNA/DNA detection by modulating device conductivity. Similarly, Gracia *et al.* (2011) covalently immobilized a chimeric fibrin–filaggrin peptide (CFFCP1) on carboxylated multi-walled CNTs (MWCNTs) *via* EDC–NHS coupling chemistry, enabling the selective detection of anti-CFFCP1 antibodies in both rabbit and human sera, with minimal response from healthy controls, demonstrating the high specificity of the peptide-functionalized sensor.[21]

Therefore, the studies developing small peptides for DENV-2 NS1 are still limited. Lim *et al.* (2018)[22] and Kim *et al.* (2019)[23] have already developed DENV-2 NS1 peptide detection tools. Lim *et al.* (2018)[22] developed some peptides by phage library approaches. On the other hand, Kim *et al.* (2019)[23] selected peptide designs from either a reverse sequence of an existing peptide, phage display, or a modified peptide with a linker. In our present work, we develop DENV-2 NS1 peptide recognition by computational approaches of sequential point mutation. Furthermore, we emphasize that the template of DENV-2 NS1 used is from the Indonesian sequence to obtain the peptide binding region. Therefore, this study identifies a novel peptide candidate for use as a DENV-2 NS1 biosensor and introduces a computational strategy that can support the optimization of DENV-peptide-based biosensor development, as illustrated in the workflow of Fig. 1.

2. Experimental section

2.1. Sequence retrieval, phylogenetic, and mutation analysis

NS1 amino-acid sequences of dengue virus serotype 2 (DENV-2) were retrieved from the NCBI GenBank database (**https://www.ncbi.nlm.nih.gov/genbank/**). To focus on locally circulating strains, only sequences from peer-reviewed studies in Indonesia were retained. Six interest sequences of DENV-2 NS1 reference from previous report by Aryati *et al.*, (2013) which has been deposited at the GenBank database.[18] FASTA files were imported into MEGA 11 (ref. 24) to construct a phylogenetic tree using the Maximum Likelihood method with default settings, except that branch support was assessed by bootstrap analysis with 500 replicates. Bootstrap values higher than 70% were considered indicative of reliable lineage assignment.

2.2. NS1 DENV-2 Indonesian strain protein modelling and structure validation

Three-dimensional model of the Indonesian NS1 DENV-2 was generated with the TrRosetta web server,[25] which integrates deep learning and homology modeling. Templates were identified by HHsearch against the RCSB PDB, yielding five high-confidence NS1 structures (PDB IDs 4TPL, 4O6D, 5GS6, 5K6K, 6WEQ; overall confidence = 100). Each model was evaluated for overall confidence score, coverage, sequence identity, *E*-value, and *Z*-score. Final NS1–DENV2 protein model was validated *via* ERRAT and Ramachandran-plot analysis in SAVES 6.0.[26]

2.3. Peptide design and structural modelling

The peptide design strategy utilized in this study refer to our previous report by Jauhar *et al.* (2024)[27] which aligns with the method described by Mastouri *et al.* (2022).[20] First, to identify a high-identity structural template of NS1 DENV-2 Indonesian strain, the sequence was queried against the Protein Data Bank

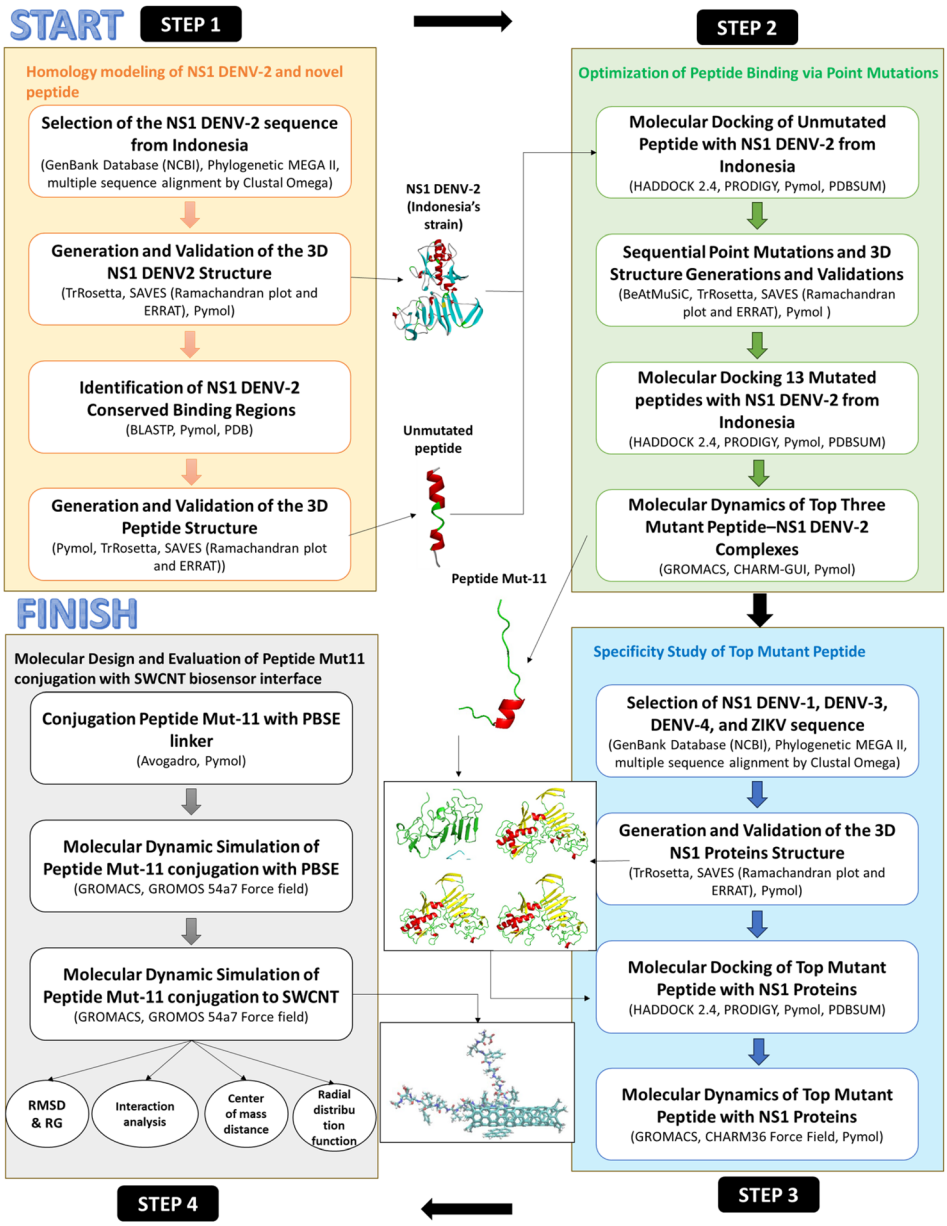

Fig. 1 Workflow outlining the computational methodology.

(PDB) using BLASTp (https://blast.ncbi.nlm.nih.gov).[28] Candidate hits were aligned to the Indonesian NS1 sequence, and complexes with ≥95% sequence identity and antibody-binding to conserved epitopes were shortlisted. Chain A of PDB ID 7BSC was selected for its high sequence identity and clear antigen–antibody interface. The structure was visualized in PyMOL (https://pymol.org/2/)[29] to map key heavy and light-chain contacts. Structural quality was then validated *via* ERRAT and Ramachandran-plot analysis using the SAVES 6.0 web server (https://saves.mbi.ucla.edu/).[26]

Active binding residues on NS1 were first identified from the 7BSC complex in PyMOL. An initial ("unmutated") peptide sequence spanning these contact points with the antibody's chains was drafted to mimic antibody interactions. Three-dimensional models were generated with the TrRosetta web server,[25] which integrates deep learning and homology modeling.

2.4. Selectivity study of peptide with NS1 virus serotypes

For the selectivity study of NS1 serotypes, we are using 48 NS1 genes of DENV serotypes 1, 3, and 4 Indonesian strain from previous report by Aryati *et al.*, (2013)[18] then repeat similar steps in 2.1.

Besides DENV, three other viruses co-circulate with dengue: zika virus (ZIKV), Yellow Fever virus (YFV), and Japanese Encephalitis virus (JEV). To determine which virus to include in this study, three selection criteria were applied: (i) belonging to the same genus (flavivirus), mosquito-borne, and secreting the NS1 protein; (ii) documented cases in Indonesia; and (iii) NS1 sequence similarity of at least 60% to DENV-2 NS1. Based on

report from the Indonesian Ministry of Health, YFV has never been reported in Indonesia and was therefore excluded. Sequence similarity was assessed using the BLASTp web server with DENV-2 NS1 as input. The BLASTp results showed that ZIKV NS1 (PDB ID: 5IY3, chain A) shared 60% similarity (109 identical residues), while JEV NS1 (PDB ID: 5O19, chain A) showed only 59% similarity (108 identical residues). Based on these findings, ZIKV NS1 was selected for further analysis. Then, similar steps in 2.5, 2.6, and 2.7 were repeated for selectivity analysis of peptide mutations.

2.5. Molecular docking

Molecular docking of the NS1 DENV-2 protein with the designed unmutated peptide was performed using the HADDOCK 2.4 web server (**https://wenmr.science.uu.nl/haddock2.4/**).[30,31] Active and passive residues at the anticipated protein–peptide interface were defined as Ambiguous Interaction Restraints (AIRs), enabling HADDOCK to sample conformations locally around the binding site rather than conducting a fully *ab initio* search. The docking protocol comprised rigid-body minimization, semi-flexible refinement, and final water refinement. Clusters of models were ranked by the HADDOCK score, which integrates intermolecular van der Waals, electrostatic, desolvation, and restraint-violation energies. For each cluster, we recorded the HADDOCK score, *Z*-score, RMSD relative to the best model, and individual energy terms. The top-scoring complexes were downloaded in PDB format for further analysis.

2.6. Interaction affinity and interface analysis

To estimate binding affinity, the highest-scoring NS1–peptide complexes were submitted to the PRODIGY web server (**https://bianca.science.uu.nl/prodigy/**) at 25 °C,[32,33] which predicts ΔG based on interfacial residue contacts. Finally, detailed noncovalent interactions and inter-atomic distances were characterized using the PDBsum Generate server (**http://www.ebi.ac.uk/thornton-srv/databases/pdbsum/Generate.html**).[34] This analysis provided a comprehensive map of hydrogen bonds, salt bridges, and hydrophobic contacts between NS1 and the peptide.

2.7. Peptide point mutation

To enhance peptide affinity and stability, specific amino acid substitutions were introduced into the unmutated NS1–peptide complex using the BeAtMuSiC web server (**http://babylone.ulb.ac.be/beatmusic/**).[35,36] BeAtMuSiC requires three inputs: (1) the PDB file of the protein–peptide complex—in this study, the NS1 DENV-2–peptide complex; (2) designation of "partner 1" and "partner 2", here assigned to NS1 and the peptide, respectively, ensuring each partner includes at least one chain in direct contact; and (3) specification of target residues for either individual mutation evaluation or systematic mutational scanning across the peptide chain. Upon submission, BeAtMuSiC computes the change in binding free energy ($\Delta\Delta G$_B) for each mutation, ranking substitutions by their predicted effect on complex stability.

2.8. Molecular dynamics simulation of NS-1 DENV-2 with peptide design

The molecular dynamics (MD) simulation was conducted using GROMACS[37] with the CHARMM36 force field.[38] Initial structural preparation involved obtaining a .pdb file of the protein–peptide complex, with individual protein and peptide files separated using PyMOL. Atom and residue names were standardized using the CHARMM-GUI PDB Reader & Manipulator web server to ensure compatibility with the CHARMM force field. Topology files were generated with 'gmx pdb2gmx', omitting hydrogen atoms and applying the TIP3P water model. Solvation was performed using a cubic simulation box (1.0 nm distance from the solute to the box edge) and SPC216 water configuration, followed by the addition of Na^+ (SOD) and Cl^- (CLA) ions to neutralize the system using the 'gmx genion' module. Energy minimization was carried out using the steepest descent algorithm for a maximum of 50 000 steps (100 ps), and the potential energy was analyzed to ensure system relaxation.

Equilibration was performed in two phases using the leap-frog integrator: NVT (constant number of particles, volume, and temperature) and NPT (constant number of particles, pressure, and temperature) ensembles. Each phase was simulated for 500 ps at 300 K and 1 atm, with system stability assessed through temperature, pressure, and density plots generated from '.xvg' files using xmgrace. Following successful equilibration, production MD simulations were executed for 25 ns (12 500 000 steps) using the 'gmx mdrun' module with GPU acceleration. The production run continued from the NPT phase checkpoint and was performed separately for each system: protein–peptide complex, protein only, and peptide only. Trajectories were analyzed every 1 ps to compute RMSD, R_g, and Center-of-Mass Distance.

2.9. Molecular dynamics simulation of SWCNT, linker, and peptide

All MD simulations were performed in GROMACS using the GROMOS 54a7 force field.[39] Systems were assembled in a cubic box with SPC water and neutralized with Na^+/Cl^- ions. Initial energy minimization employed the steepest-descent algorithm until the maximum force fell below 1000 kJ mol^{-1} nm^{-1}. Equilibration proceeded in two phases:

Phase I: the peptide was conjugated to PBSE and subjected to 100 ps NVT equilibration at 300 K (V-rescale thermostat) followed by 100 ps NPT equilibration at 1 bar (Parrinello–Rahman barostat).

Phase II: the equilibrated peptide–PBSE complex was placed near the CNT surface, and the system underwent the same NVT/NPT equilibration protocol.

Production runs of 10 ns were conducted under NPT conditions with a 2 fs time step. Long-range electrostatics were treated with Particle-Mesh Ewald (1.2 nm cutoff), and van der Waals interactions used a 1.2 nm cutoff. Trajectories were analyzed every 1 ps to compute RMSD, R_g, and Center-of-Mass Distance.

3. Results

3.1. Selection of a conserved NS1 DENV-2 sequence originated from Indonesia

In this study, NS1 gene sequences of dengue virus serotype 2 (DENV-2) originating from Indonesia were retrieved from the GenBank database (NCBI) to facilitate the rational design of a peptide-based biosensor. Six sequences were selected based on a report by Aryati *et al.* (2013)[18] which provided NS1 DENV-2 gene data from diverse geographical regions across Indonesia, including Semarang, Jakarta, Medan, and Surabaya. (Table S1, SI data). To identify a representative target for structural modeling and peptide design, we performed phylogenetic and mutation analyses.

A phylogenetic tree was constructed using MEGA 11 with the Maximum Likelihood method. As shown in Fig. 2, sequences AHK09923.1, AHK09924.1, and AHK09925.1 clustered within the outermost clade, indicating ancestral origin and high sequence conservation. This indicates that these sequences are more likely to reflect conserved structural features relevant for stable and broad-spectrum peptide binding.

To select the most suitable target for computational modeling, amino acid variations among the three sequences were analyzed using MEGA 11. Sequence AHK09925.1 showed no amino acid differences relative to the others, confirming its status as the most conserved (Fig. 2). Therefore, AHK09925.1 was selected as the reference sequence for subsequent structural modeling.

3.2. NS1 DENV-2 protein modelling and structure validation

The 3D structure of the NS1 DENV-2 protein from Indonesia was predicted using the trRosetta web server, based on the input sequence AHK09925.1. This tool integrates deep learning with homology modeling, utilizing structural templates from the Protein Data Bank (PDB) identified *via* HHSearch. Five PDB structures were selected as templates, each with a 100% confidence score: 4TPL (Chain B), 406D (Chain A), 5GS6 (Chain A), 5K6K (Chain A), and 6WEQ (Chain B). The resulting model exhibited strong homology, as evidenced by a high TM-score (0.948) indicating a reliable and accurate structural prediction.

Five templates identified *via* HHSearch from the PDB were used, each with a confidence score of 100, indicating a very high likelihood of true-positive matches. The coverage values were above 90, and the identity values exceeded 50%, meaning the predicted structure closely resembles the real protein. A low *E*-value (below 0) and a high *Z*-score further indicate that the prediction is highly reliable and unlikely to be due to chance. Finally, the estimated TM-score of 0.948 strongly supports the reliability of the predicted model.

Following model construction, the structure was visualized and analyzed using PyMOL. Fig. 3a shows the secondary structure of the NS1 DENV-2 protein, characterized by α-helices (red), β-sheets (cyan), and loops (white). Validation through Ramachandran plot analysis indicated that 91.6% of the residues were located in the most favorable region, 7.4% in the additionally allowed region, and 1% in the generously allowed region, with no residues in the disallowed region. The ERRAT

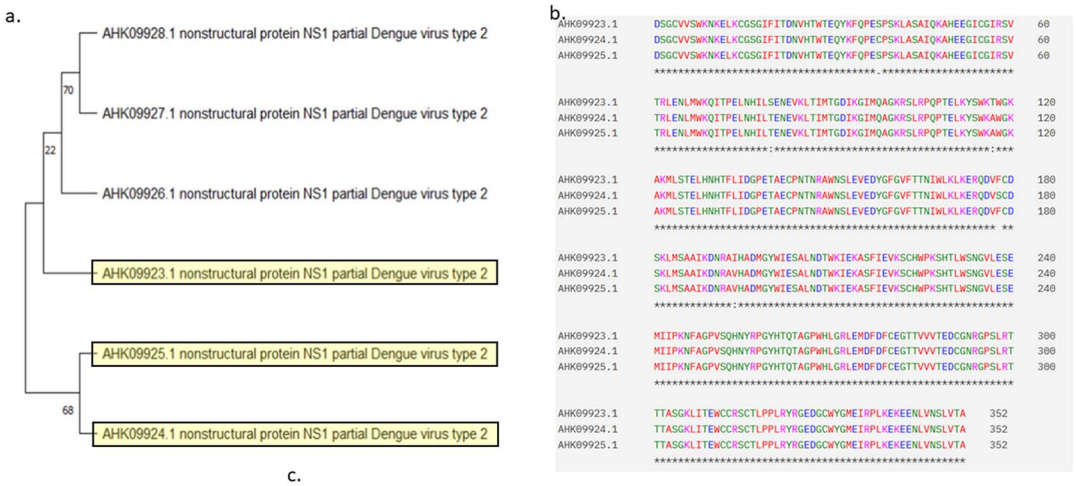

Sequences	Residue number					Mismatch residues
	38	80	117	178	194	
AHK09923.1	S	S	T	F	I	3
AHK09924.1	C	T	A	S	V	2
AHK09925.1	S	T	A	F	V	0

Fig. 2 Phylogenetic relationship and multiple sequence alignment of NS1 protein sequences from dengue virus serotype 2 (DENV-2). (a) Phylogenetic tree constructed using full of NS1 protein sequences of DENV-2 (accession numbers: AHK09928.1, AHK09927.1, AHK09926.1, AHK09923.1, AHK09925.1, and AHK09924.1). The tree illustrates the evolutionary relationships among the sequences, with bootstrap values shown at the nodes. (b) Multiple sequence alignment of the same NS1 protein sequences, highlighting conserved and variable amino acid residues. Identical residues are marked with asterisks (*), and color coding indicates physicochemical properties of amino acids (*e.g.*, hydrophobic, polar, acidic, basic). The alignment was used to support phylogenetic clustering and assess sequence similarity. (c) Position of residue differences in three selected DENV-2 NS1 protein sequences (AHK09928.1, AHK09926.1, and AHK09924.1). Distinct amino acid residues identified from the multiple sequence alignment are highlighted in red.

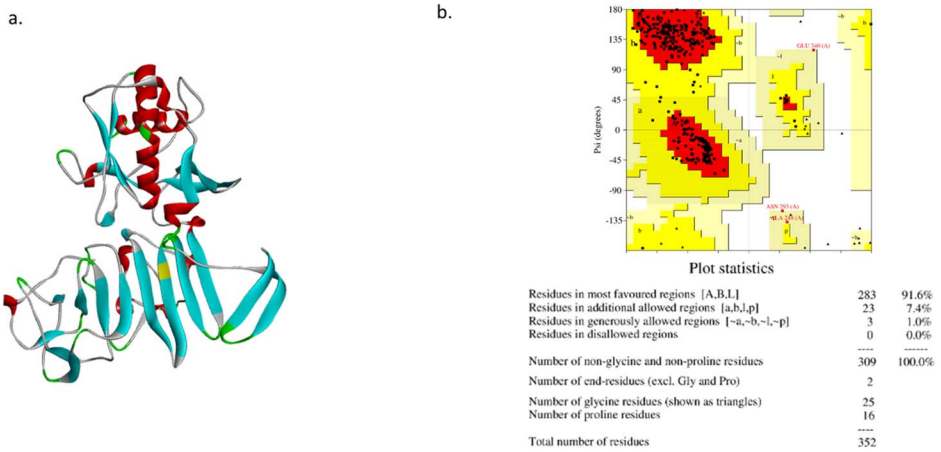

Fig. 3 3D structure and validation of the NS1 Protein from DENV-2 (a) predicted 3D model of the NS1 protein, showing secondary structure elements (α-helices in red, β-sheets in cyan, loops in grey). (b) Ramachandran plot analysis of the modeled structure. Most residues (91.6%) are in the most favored regions, indicating good stereochemical quality. Plot statistics are summarized in the table.

score for the model was 83.5526 (Fig. 3b). Thus, this NS1 DENV2 3D structure was used as the target receptor for biosensing in this study.

3.3. Identification of conserved binding regions for rational peptide design

To design a short peptide that binds specifically and strongly to the target receptor for biosensing, we used a design strategy based on our previous work Jauhar *et al.* (2024)[27] which aligns with the method described by Mastouri *et al.* (2022).[20] This strategy extracts the binding region of the target protein and converts it into a short peptide with enhanced stability and affinity through point mutations.

In this study, to identify the binding region of the target protein, we first searched for a crystal structure of the target sequence in the Protein Data Bank (PDB) by aligning the AHK09925.1 sequence using the BLASTp webserver. A threshold of >95% identity was applied, prioritizing structures complexed

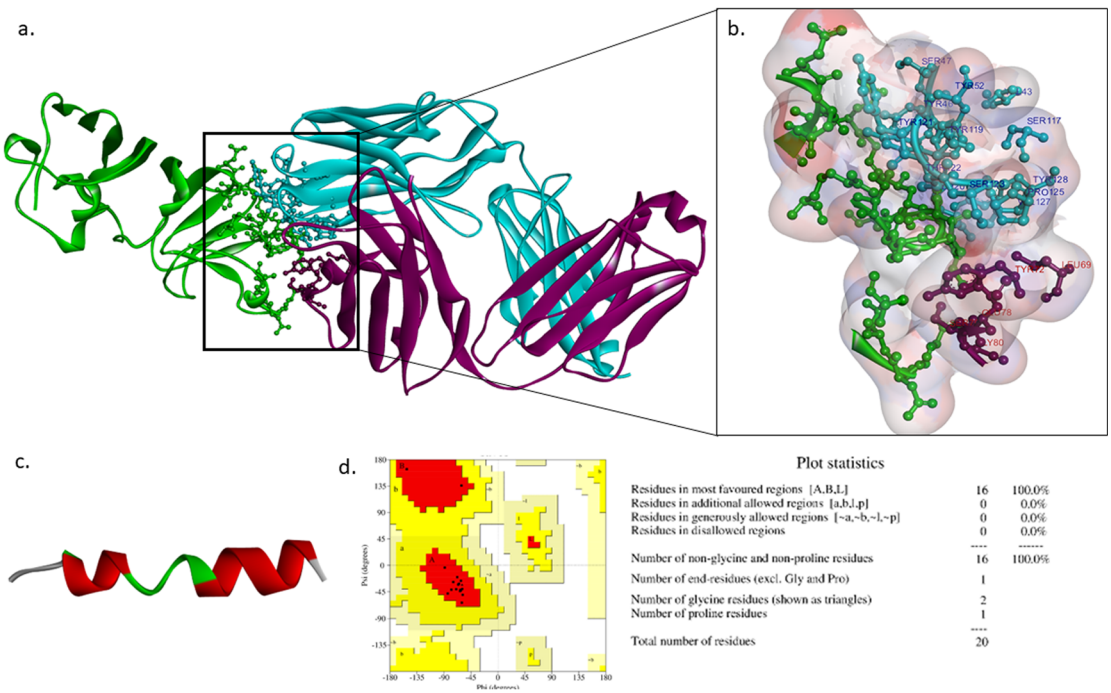

Fig. 4 Conserved binding site and peptide design for NS1 target interaction. (a) Predicted binding site on the NS1 protein (colored domains) with the designed peptide (green) shown interacting at the conserved region (highlighted box). (b) Close-up view of the binding interface showing key interacting residues and surface representation. (c) 3D structure of the designed peptide. (d) Ramachandran plot validation of the peptide structure, with all residues (100%) in the most favored regions, indicating a reliable model.

with antibodies, which typically bind to conserved regions. Result revealed a highly similar structure of PDB ID: 7BSC (Chain A) that exhibits 99% identity, with 179 out of 181 amino acids being identical. This structure, which represents the antigen-binding fragment (Fab) of monoclonal antibody 1G5.3 complexed with the C-terminal fragment of NS1 (NS1c) from DENV-2, was employed for subsequent structural analysis.

The NS1c domain is shown in green in Fig. 4a, with the antibody heavy chain in cyan and the light chain in magenta. Structural analysis using PyMOL revealed that the active site of the target protein interacts with the heavy chain at residues 20E, 43V, 45G, 46Y, 47S, 117S, 52Y, 119Y, 121Y, 128Y, 122T, 123S, 125P, and 127V (Fig. 4b). While, interactions with the light chain were observed at residues 69L, 72Y, 78E, 79S, and 80G. Based on these binding regions, a peptide sequence was constructed by combining residues from both heavy and light chain contact sites, hereafter referred to as the unmutated peptide (Fig. 4c).

3.4. Unmutated peptide modelling with structure validation

The unmutated peptide sequence, EVGYSSYYYYTSPVYLYESG, was modelled using the trRosetta web server. Due to the novel nature of this peptide and the absence of suitable structural templates, *de novo* folding guided by deep learning-based restraints was applied. As a result, the model yielded a low TM-score of 0.177, indicating limited structural similarity to known proteins, yet sufficient for preliminary structural assessment. The predicted structure, visualized in PyMOL, consisted of α-helices (red) and loops (green) (Fig. 4c). Structural validation using a Ramachandran plot showed that 100% of residues were located in the most favorable regions, with no residues in disallowed regions. Furthermore, the model achieved an ERRAT score of 100, supporting the reliability of the predicted structure (Fig. 4c).

3.5. Molecular docking and interaction analysis of unmutated peptide

Molecular docking of the unmutated peptide to the active site of the NS1 DENV-2 protein was performed using the HADDOCK 2.4 web server to assess the peptide's binding affinity and interaction strength. The NS1 DENV-2 protein consists of three major domains: the hydrophobic β-roll domain (amino acids 1–29), which facilitates dimerization; the wing domain, comprising connector subdomains (residues 30–37 and 152–180) and an α/β subdomain (residues 38–151); and the β-ladder domain spanning residues 181–352.[40] Additionally, Modhiran *et al* (2015)[41]. reported that key active residues within the β-ladder domain of NS1 DENV-2 play a critical role in binding to conserved antigenic regions. The molecular docking simulation resulted in HADDOCK score of -39 ± 3.3, with binding energy (ΔG) of -11.2 kcal mol^{-1} and a dissociation constant (K_d) of 5.8×10^{-9} M at 25 °C. The unmutated peptide was observed to bind within the β-ladder domain, as shown in Fig. 5a. Furthermore, PDBsum webserver was utilize to analyze their molecular interactions.

Fig. 5b illustrates the intermolecular interactions within the peptide–NS1 complex, including hydrogen bonds, van der Waals contacts, and salt bridges. A total of seven hydrogen

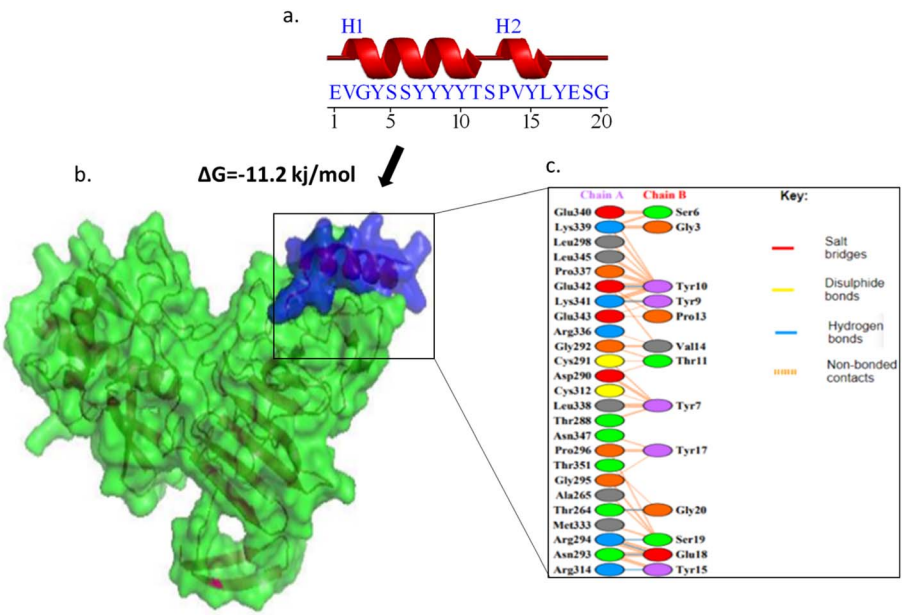

Fig. 5 Interaction model of unmutated peptide with NS1 DENV-2 protein. The unmutated peptide sequence (EVGYSSYYYYTSPVYLYESG) contains two α-helical regions (H1 and H2) as shown in the secondary structure diagram (a). The 3D molecular docking visualization (b) shows the binding orientation of the peptide (blue/purple surface) at the interface of the NS1 protein (green surface). The boxed region highlights the peptide docking site. A schematic interaction map illustrates molecular interactions between the wild-type peptide (Chain B) and NS1 DENV-2 (Chain A) (c). Various interaction types are indicated: salt bridges (red lines), hydrogen bonds (blue lines), and non-bonded contacts (orange lines). Residue–residue interactions are labeled and color-coded according to their chain origin and interaction type.

Table 1 Hydrogen bond interactions of unmutated peptide with NS1

Residues involved		
NS1	Peptides unmutated	Distance (Å)
Thr264	Gly20	2.70
Asn293	Glu18	2.66
Arg294	Glu18	2.86
Arg294	Ser19	2.81
Arg314	Tyr15	3.11
Lys341	Tyr9	2.93
Glu342	Tyr10	2.75

bonds and 149 van der Waals contacts were identified, while no salt bridges were detected. Multiple residues from the unmutated peptide, specifically Gly20, Glu18 (twice), Ser19, Tyr15, Tyr9, and Tyr10, formed strong hydrogen bonds with residues located in the β-ladder domain of NS1 DENV-2 (Fig. 5c). These interactions, coupled with the short average hydrogen bond distances (Table 1), suggest a stable binding interface and strong affinity of the peptide for the target site.

3.6. Peptide point mutations and validation

To enhance the binding affinity and overall quality of unmutated peptide, point mutations were introduced using the BeAtMuSiC web server. This approach involves substituting one or two residues within the peptide sequence to improve its interaction strength and structural stability with the target receptor (NS1 DENV-2).[35,36] Subsequently, molecular docking and molecular dynamics simulations were carried out to identify the most favorable peptides.

A total of five single-point mutant peptides were initially generated, each featuring a single amino acid substitution. Subsequently, double-point mutations were introduced, resulting in a total of 13 mutant peptides (Table 2). The 3D structures of these peptides were predicted using the trRosetta web server, following the same protocol as described previously. Structural validation was performed using the SAVES v6.0 web server, which includes Ramachandran plot analysis to evaluate stereochemical quality (Table S2. SI data). Binding potential was further assessed through ERRAT scores, reflecting overall model reliability. Based on Ramachandran plot results, Mutants 3 and 9 exhibited 5.9% of residues in disallowed regions, indicating suboptimal structural quality, and were thus excluded from further analysis. Although Mutant 7 displayed acceptable structural conformation, its ERRAT score could not be retrieved due to a server-side error, leading to its exclusion from subsequent docking validation. Therefore, only 10 of mutant peptides were used for subsequent analysis.Molecular docking and molecular dynamic simulation of NS-1 DENV-2 with Mutant Peptides.

Molecular docking of ten mutant peptides with NS-1 DENV-2 were conducted using HADDOCK webserver. In general, the mutant peptides demonstrated improved binding affinity than unmutated peptide toward the target protein, except for Mut 1 and Mut 8. Binding affinity was evaluated based on the dissociation constant (K_d), where lower K_d values reflect stronger binding interactions along with low value of binding free energies (ΔG). Among the tested mutant peptides, Mut 11, Mut 10, and Mut 13 exhibited the highest binding affinities (Table 3). The K_d values of these three peptides were substantially lower than that of unmutated peptide, suggesting a significant enhancement in binding. These findings were consistent with their more favorable predicted binding free energies (ΔG) and a higher number of hydrogen bond interactions. The molecular interactions between each peptide and the NS-1 protein of DENV-2 were visualized in Fig. 6. Subsequently, the top three mutant peptides with the lowest value predicted binding affinities were selected for molecular dynamics simulation to further evaluate the stability of their interactions.

The molecular dynamics simulation was conducted by GROMACS software. The simulation was subjected to four systems: protein NS1, complex protein NS1 with Mut10 peptide (NS1–Mut10), complex protein NS1 with Mut11 (NS1–Mut11), and complex protein NS1 with Mut13 (NS1–Mut13). The result was displayed as Root Mean Square Deviation (RMSD), Root

Table 2 ERRAT and Ramachandran sequence mutation assessment

			Ramachandran			
Peptide	Sequens	ERRAT	Core	Allow	Gener	Dissall
Mut 1	EVLYSSYYYYTSPVYLYESG	100	100.0%	0.0%	0.0%	0.0%
Mut 2	EVGYSSYKYYTSPVYLYESG	72.727	100.0%	0.0%	0.0%	0.0%
Mut 3	EVYYSSYYYYTSPVYLYESG	100	82.4%	11.8%	0.0%	5.9%
Mut 4	EVGYSSYEYYTSPVYLYESG	100	100.0%	0.0%	0.0%	0.0%
Mut 5	EVGYSSYYYYTSPVYLYEWG	100	100.0%	0.0%	0.0%	0.0%
Mut 6 (Mut1+Mut2)	EVLYSSYKYYTSPVY LYESG	100	94.1%	5.9%	0.0%	0.0%
Mut 7 (Mut1 + Mut4)	EVLYSSYEYYTSPVYLYESG	ERROR	94.1%	5.9%	0.0%	0.0%
Mut 8 (Mut1 + Mut5)	EVLYSSYYYYTSPVYLYEWG	91.667	100.0%	0.0%	0.0%	0.0%
Mut 9 (Mut2 + Mut3)	EVYYSSYKYYTSPVYLYESG	100	88.2%	5.9%	0.0%	5.9%
Mut 10 (Mut2 + Mut5)	EVGYSSYKYYTSPVYLYEWG	100	100.0%	0.0%	0.0%	0.0%
Mut 11 (Mut3 + Mut4)	EVYYSSYEYYTSPVYLYESG	100	94.1%	5.9%	0.0%	0.0%
Mut 12 (Mut3 + Mut5)	EVYYSSYYYYTSPVYLYEWG	100	94.1%	5.9%	0.0%	0.0%
Mut 13 (Mut4 + Mut5)	EVGYSSYEYYTSPVYLYEWG	100	100.0%	0.0%	0.0%	0.0%

Table 3 Molecular docking result of sequence mutation with NS-1 DENV-2

Peptide	HADDOCK score	ΔG	K_d (25°C)	H bonds	Salt bridges	Non bonded contacts
Unmutated	−39 ± 3.3	−11.2	5.8×10^{-9}	7	0	149
Mut1	−41.3 ± 3.8	−10.4	2.2×10^{-8}	11	1	133
Mut2	−49.9 ± 5	−11.8	2.2×10^{-9}	8	0	132
Mut4	−41.2 ± 14.9	−11.7	2.7×10^{-9}	13	1	184
Mut5	−49.4 ± 7.4	−12.2	1.0×10^{-9}	8	1	136
Mut6	−48.4 ± 9.1	−11.8	2.1×10^{-9}	12	0	117
Mut8	−44.7 ± 11.6	−10.9	9.6×10^{-9}	6	1	138
Mut10	−74.8 ± 10.4	−12.7	5.0×10^{-10}	14	1	157
Mut11	−77.9 ± 8.3	−12.5	7.2×10^{-10}	11	0	152
Mut12	−68.7 ± 3.4	−12.2	1.1×10^{-9}	6	0	107
Mut13	−68.7 ± 3.4	−13	2.9×10^{-10}	8	2	139

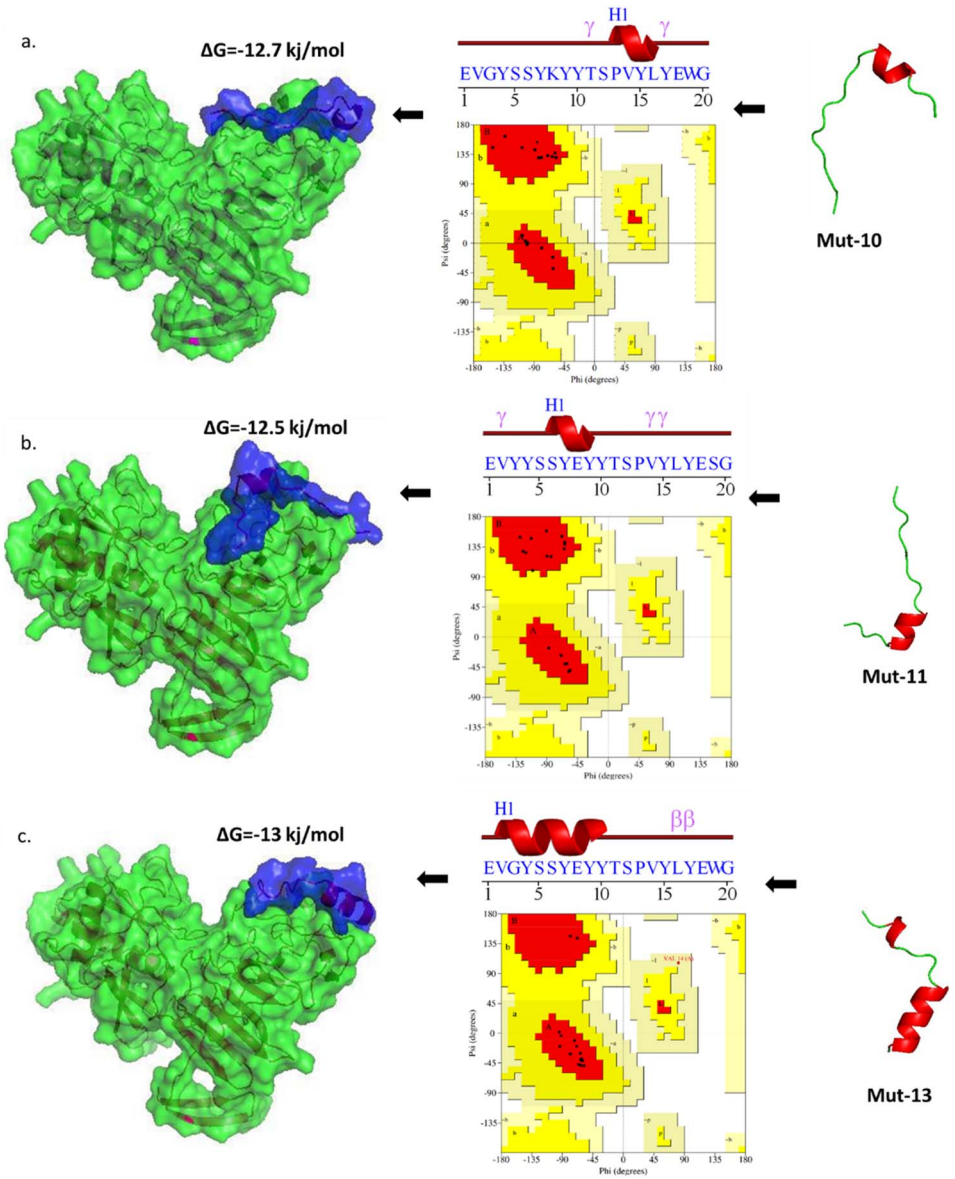

Fig. 6 Structural comparison and conformational analysis of peptide mutants docked to NS1 DENV-2.Docking and structural evaluation of three peptide mutants: (a) EVGYSSKYYTSPVYLEWG ($\Delta G = -12.7$ kJ mol^{-1}), (b) EVVYSSYEYYTSPVYLESG ($\Delta G = -12.5$ kJ mol^{-1}), (c) EVGYSSYEYYTSPVYLEWG ($\Delta G = -13$ kJ mol^{-1}).Each panel shows the docked complex (left), predicted secondary structure and Ramachandran plot (middle), and the free peptide conformation (right). Differences in binding affinity, torsional angles, and secondary structure content are highlighted.

Mean Square Fluctuation (RMSF), Radius of Gyration (R_g), and Solvent Accessible Surface Area (SASA) during 25 ns simulation.

As shown in Fig. 7a, most complexes exhibited notable RMSD fluctuations of up to 0.6 nm during the first 16 ns of the simulation. In contrast, the NS1–Mut11 complex maintained greater structural stability, with RMSD values remaining below 0.3 nm throughout the same period, showing only slight fluctuations after 17 ns. Beyond 18 ns, all complexes stabilized, with no significant fluctuations observed up to 25 ns. Notably, the NS1–Mut11 complex exhibited the lowest average RMSD value of 0.273 nm (Table 4), indicating it as the most stable complex among others.

The RMSF profiles of all NS1–Mutant peptide complexes are presented in Fig. 7b. A consistent pattern of high atomic fluctuations was observed at the N-terminal region of the NS1 protein across all complexes. However, this analysis specifically focused on the key binding site residues: E281, G282, R299, T301, T302, A303, S304, G305, K306, L307, T309, E326, D327, G328, C329, E343, N344, L345, and S348 which are involved in peptide interaction. These residues exhibited relatively low RMSF values, all below 0.2 nm (2 Å), indicating limited flexibility. This suggests that the binding site residues remain structurally stable upon interaction with the mutant peptides, supporting the stability of the protein-mutant peptide complexes.

Fig. 7c shows that all four simulation systems reached a relatively stable structure after 10 ns. The NS1–Mut10 and NS1–Mut11 complexes displayed more stable radius of gyration (R_g) curves compared to the free NS1 protein and NS1–Mut13 complex. The average R_g values for all systems ranged from 2.31 to 2.40 nm, indicating stable structural compactness. Similarly, the solvent-accessible surface area (SASA) curves in Fig. 7d showed the same trend, with all systems stabilizing after 10 ns. The average SASA values ranged from 186 to 216 nm^2.

Table 4 Molecular dynamics result average

Name	RMSD	R_g	SASA
NS1	0.365 ± 0.830	2.368 ± 0.026	194.310 ± 3.112
NS1–Mut10	0.377 ± 0.066	2.398 ± 0.020	199.247 ± 4.580
NS1–Mut11	0.273 ± 0.051	2.400 ± 0.017	199.802 ± 4.599
NS1–Mut13	0.426 ± 0.067	2.428 ± 0.027	205.660 ± 4.602

3.7. Specificity study of mutated peptide with DENV-1, DENV-3, DENV-4 and zika virus (ZIKV)

The NS1 sequences of Indonesian DENV-1, DENV-3, and DENV-4 used for specificity study were retrieved from the same source as DENV-2 (ref. 18) and selected based on their closest phylogenetic relationship to the Indonesian DENV-2 strain. After constructed a maximum-likelihood tree (Fig. S1), we chose those NS1 sequences that clustered in the same clade and resulting in choosing AHK09904.1 (DENV-1), AHK09933.1 (DENV-3), and AHK09949.1 (DENV-4).

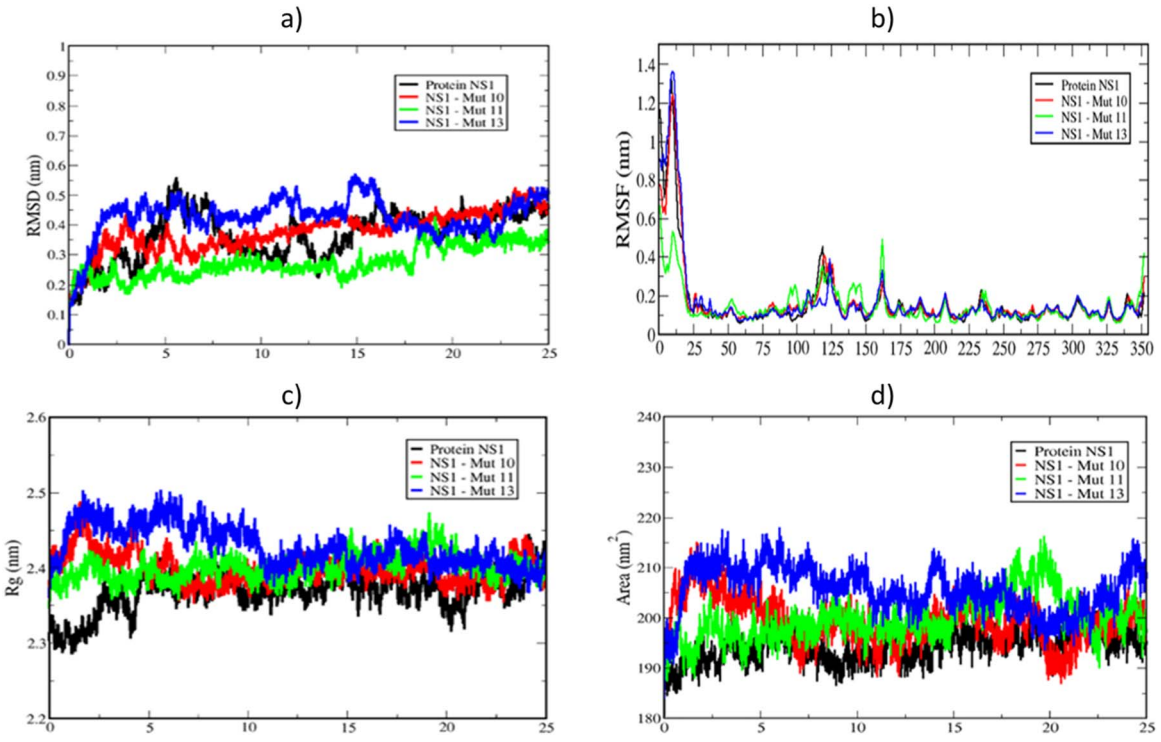

Fig. 7 Molecular dynamics analysis of NS1–peptide mutant complexes over 25 ns. (a) RMSD (Root Mean Square Deviation) plot showing structural stability. (b) RMSF (Root Mean Square Fluctuation) plot showing residue flexibility. (c) Radius of gyration (R_g) indicating protein compactness. (d) Solvent Accessible Surface Area (SASA) representing surface exposure. Protein NS1 (black), Mutant 10 (red), Mutant 11 (green), and Mutant 13 (blue) are compared.

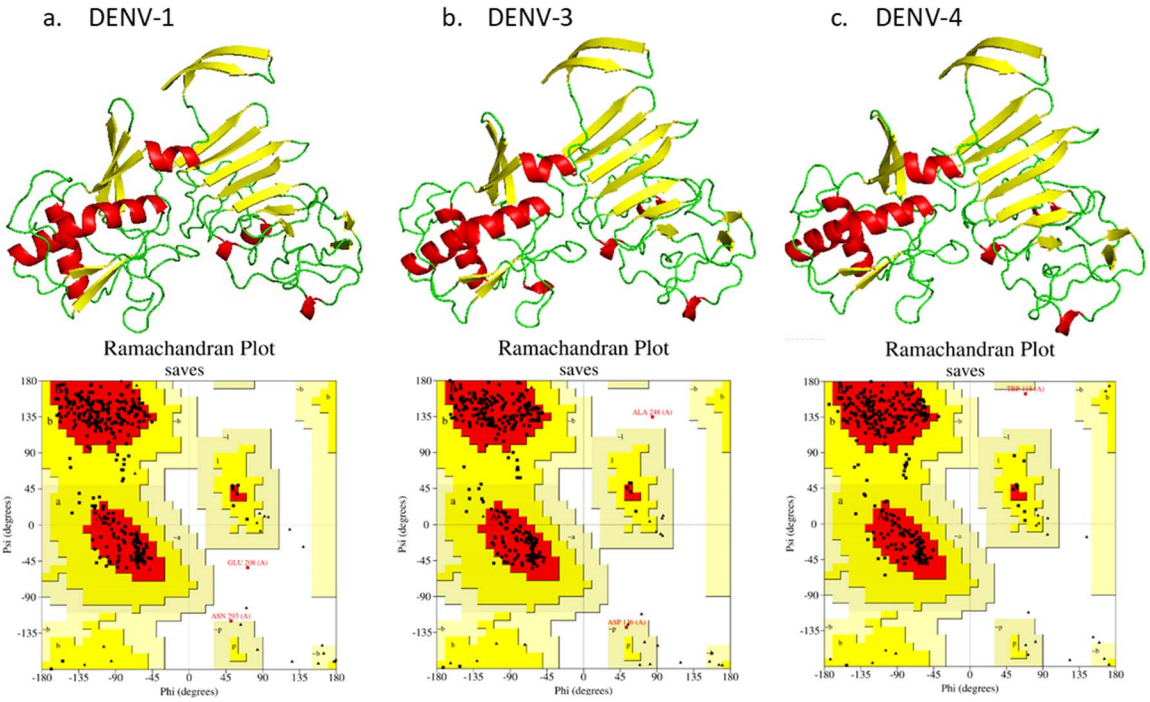

Fig. 8 Homology models and Ramachandran plots of NS1 proteins from DENV-1 (a), DENV-3 (b), and DENV-4 (c) generated using trRosetta. Top: 3D structures showing well-formed α-helices (red) and β-sheets (yellow).Bottom: Ramachandran plots confirming good model quality, with >90% residues in favored regions and only a few outliers, indicating suitability for further analysis.

Homology models for these three dengue serotypes were generated using the trRosetta web server and validated by Ramachandran plot and ERRAT analyses. The ERRAT quality factors were 89.23 for DENV-1, 87.92 for DENV-3, and 88.75 for DENV-4. In each case, fewer than two residues (which were non-active residues) occupied disallowed regions, while over 90% of residues fell within favored regions of the Ramachandran plot.

These validation results confirm that these dengue NS1 models are suitable for binding-specificity study (Fig. 8).

To evaluate potential cross-reactivity with non-dengue flaviviruses, we performed a BLASTp search of the DENV-2 NS1 sequence against the PDB. Zika virus NS1 (PDB ID: 5IY3, chain A) emerged with 60% sequence identity over the full 109-residue length and was therefore included in our specificity study.

Prior to molecular docking of peptide Mut-11 with the four NS1 proteins, active sites were predicted using the FTsite web server. Docking simulations were then carried out in HADDOCK, and the resulting complexes were evaluated for binding free energy (ΔG) and dissociation constant (K_d) at 25 °C *via* the PRODIGY web server. The binding specificity results are summarized in Table 5.

These data show that Mut-11 binds most strongly to DENV-2 NS1, with a binding free energy ΔG of -12.5 kJ mol^{-1} and the lowest dissociation constant (K_d) among all dengue serotypes, as well as the highest number of hydrogen bonds, salt bridges, and hydrophobic contacts at the interface. Although the ΔG and K_d values for DENV-1, DENV-3, and DENV-4 were only marginally less favorable, Mut-11's affinity for ZIKV NS1 was substantially weaker ($\Delta G = -9.4$ kJ mol^{-1}), accompanied by markedly fewer inter-molecular contacts. These findings confirm that Mut-11 is highly specific for dengue NS1 and discriminates effectively against the zika virus homologue. Therefore, Molecular dynamics study were further analyzed.

Fig. 9 illustrates the RMSD profiles of peptide Mut-11 in complex with NS1 proteins from various flaviviruses. The DENV-1 complex exhibited substantial fluctuations, reaching up to ~1.0 nm (10 Å), with an average RMSD of 0.580 ± 0.130 nm, indicating structural instability. Similarly, the ZIKV complex

Table 5 Binding affinity and interaction analysis of peptide Mut-11 with NS1 proteins from DENV serotypes and ZIKV

Sequens	HADDOCK score	ΔG	K_d (at 25 °C)	Total of H-Bonds	Total of salt bridges	Non-Bonded Contact
DENV-2	-77.9 ± 8.3	-12.5	7.2×10^{-10}	11	0	152
DENV-1	-123.3 ± 2.9	-10.5	2.1×10^{-8}	9	1	125
DENV-3	-133.1 ± 4.7	-10.7	1.5×10^{-8}	10	2	110
DENV-4	-115.5 ± 1.5	-10.3	3.0×10^{-8}	6	0	104
ZIKV	-107.5 ± 7.4	-9.4	1.3×10^{-7}	10	1	119

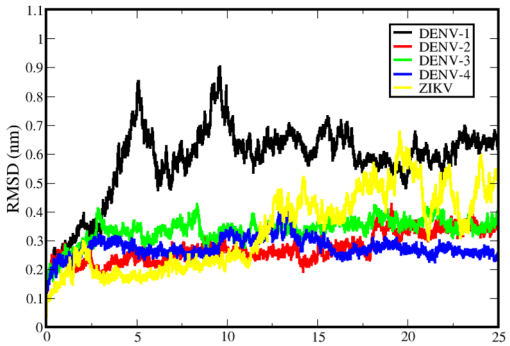

Fig. 9 RMSD of peptide Mut-11 in complex with NS1 proteins from DENV-1 (black), DENV-2 (red), DENV-3 (green), DENV-4 (blue), and ZIKV (yellow) over a 25 ns molecular dynamics simulation.

showed elevated deviations beyond 10 ns of simulation, peaking near 0.7 nm (7 Å) with a mean RMSD of 0.333 ± 0.137 nm. These observations suggest that peptide Mut-11 dissociates under dynamic conditions when bound to NS1 from DENV-1 and ZIKV.In contrast, complexes with DENV-2, DENV-3, and DENV-4 exhibited more stable RMSD profiles throughout the simulation, with average values of 0.273 ± 0.051 nm, 0.336 ± 0.043 nm, and 0.275 ± 0.034 nm, respectively. Supporting analyses of RMSF, radius of gyration (R_g), and solvent-accessible surface area (SASA) across all five systems (Fig. S2–S4) confirmed these trends. Collectively, these results underscore the specificity of peptide Mut-11 toward DENV-2 NS1, with sustained binding also observed for DENV-3 and DENV-4, while exhibiting selective non-binding behavior toward DENV-1 and ZIKV.

Structural snapshots at 0 ns, 12.5 ns, and 25 ns were extracted and visualized (Fig. 10) to assess conformational changes in the peptide–protein complexes. Fig. 10 illustrates the stability and conformational behavior of the peptide–NS1 protein complexes under dynamic conditions. Peptide Mut-11 remained stably bound to DENV-2, DENV-3, and DENV-4 NS1 proteins throughout the simulation, exhibiting minimal displacement. In contrast, notable conformational drift and partial detachment of the peptide were observed in the DENV-1 and ZIKV complexes, suggesting reduced binding stability and potential selectivity of Mut-11 for dengue NS1 over zika NS1.

3.8. Molecular dynamic simulation of potential biosensor system for detecting NS1 DENV-2

To support the design of a potential biosensor system in this study, we evaluated a potential substrate material that enables strong surface binding of the selected mutant peptide (Mut11). PBSE (*p*-aminobenzoic acid succinimidyl ester) was employed as a conjugating linker to facilitate peptide attachment to the substrate. Previous work by Badhe *et al.* (2021)[42] demonstrated that PBSE effectively stabilizes peptides on single-walled carbon nanotube (SWCNT) surfaces and is widely used in biosensing applications. Therefore, this section focuses on assessing the interaction between the PBSE-conjugated Mut11 peptide and SWCNT using molecular dynamics (MD) simulations. Prior to the MD simulations, energy minimization, system equilibration and system running were conducted in two sequential phases: Phase I and Phase II. In Phase I, the Mut 11 peptide was conjugated with the PBSE linker. In Phase II, the PBSE-conjugated Mut 11 peptide was simulated in interaction with the SWCNT to predict the potential of the system for biosensor applications.

The successful energy minimization in both Phase I and Phase II was indicated by negative potential energy values on the order of 10^5, with values of −407 214.375 kJ mol^{-1} and −1 025 140.5 kJ mol^{-1}, respectively. Equilibration under NVT (constant number of particles, volume, and temperature) conditions was confirmed by average temperatures close to the target of 300 K (300.010 ± 2.007 K for Phase I and 299.937 ± 1.276 K for Phase II), with fluctuations below ±5 K. Under NPT (constant number of particles, pressure, and temperature) conditions, system stability was supported by consistent densities (979.395 ± 3.020 kg m^{-3} for Phase I and 979.135 ± 1.935 kg m^{-3} for Phase II), approaching the reference value for the SPC water model that is 998 kg m^{-3}.[43] These results confirm that both systems were successfully equilibrated and ready for production MD simulations.

Fig. 11 shows the conformation of the conjugated peptide before and after the 10-nanosecond (ns) molecular dynamics (MD) simulation. The left image represents the peptide structure at the beginning of the simulation (0 ns), while the right image shows the structure after 10 ns. Initially, the conjugated peptide appears more extended and less folded. This is expected, as peptide Mut 11 contains active binding sites for the NS1 protein of DENV-2, involving five key amino acids: Glu1, Tyr3, Ser12, Tyr17, and Ser19. It is essential that the PBSE linker does not bind to these critical residues. The MD simulation results showed that throughout the 10 ns duration, the PBSE linker remained stably attached to Glu8 and Glu18, avoiding the functional binding sites. By the end of the simulation, the peptide adopted a more folded conformation, suggesting enhanced structural stability through internal interactions, such as hydrogen bonding. This folding behavior indicates that the conjugated peptide achieves a more energetically favorable and stable conformation during the simulation.

As shown in Fig. 12a, the RMSD values range from 0.4 nm to approximately 0.8 nm. Notable fluctuations were observed during the initial phase of the simulation, up to around 4000 ps. After this point, the RMSD graph stabilizes, with values ranging between 0.6 and 0.7 nm until the end of the 10 ns simulation. In overall, the average RMSD was 0.676 nm, with a standard deviation of 0.116 nm.

As shown in Fig. 12b, R_g values of Phase I range from 1.2 nm to approximately 1.6 nm. The initial period, up to around 2000 ps, exhibits high fluctuations, which may reflect the early structural adjustment phase. Following this, the R_g values stabilize within the range of 1.2 to 1.4 nm until the end of the 10 ns simulation. In overall, the average R_g was 1.394 nm with a standard deviation of 0.113 nm.

In Phase II of the MD simulation, SWCNT was used as the candidate substrate material for the biosensor system designed to detect NS1 of DENV-2 using the Mut 11 peptide. Therefore,

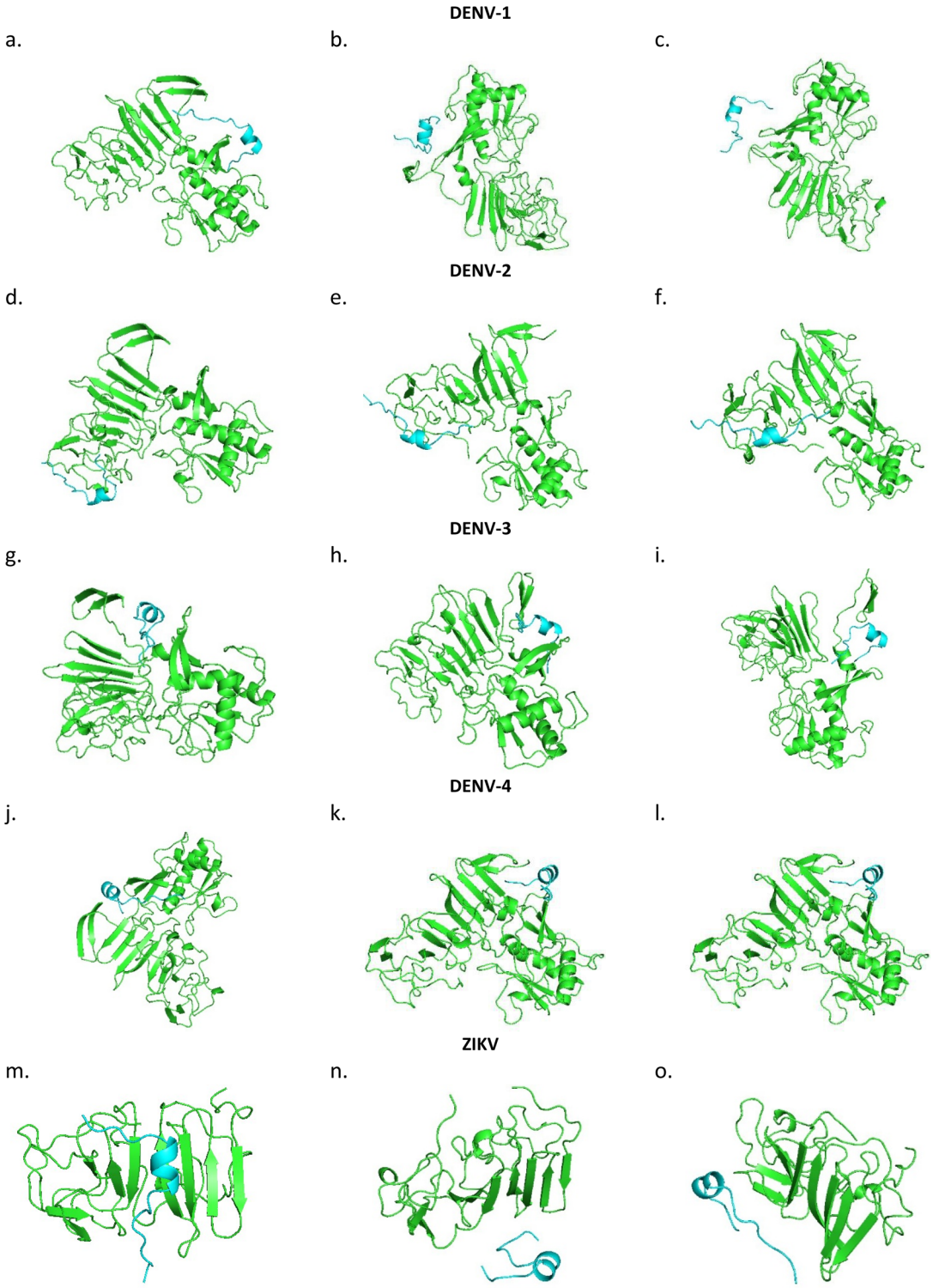

Fig. 10 Structural changes of peptide Mut-11 (blue) in complex with NS1 proteins (green) from five flaviviruses over the course of molecular dynamics simulations. Each row represents one NS1 viral target: (a–c) DENV-1, (d–f) DENV-2, (g–i) DENV-3, (j–l) DENV-4, and (m–o) ZIKV. Snapshots are shown at three time points: left (0 ns), middle (12.5 ns), and right (25 ns), respectively.

following the successful results of Phase I, the simulation was continued in Phase II with CNT incorporated as the biosensor substrate.

Fig. 13 showed that the conformational changes of the conjugated peptide with SWCNT before and after a 10 nanosecond (ns) molecular simulation, from front and side views, respectively. Initially (0 ns), the peptide appears more open and

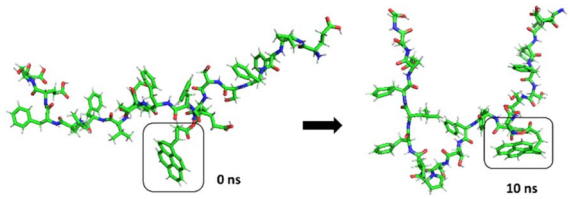

Fig. 11 Conformational shift of the conjugated peptide during 10 ns MD simulation. Structural rearrangement highlights the dynamic behavior of the pyrene-labeled peptide, with boxed regions showing significant folding or interaction changes over time.

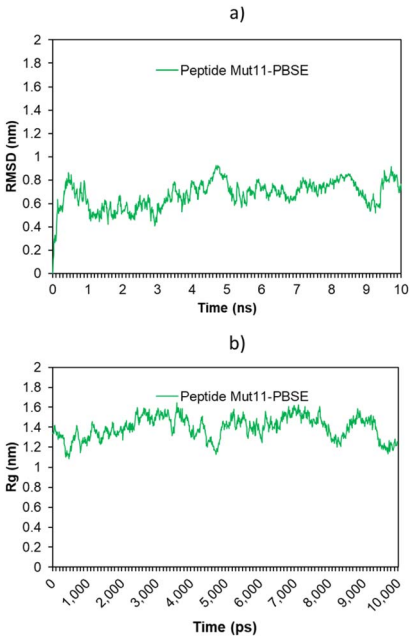

Fig. 12 Molecular dynamics simulation of conjugated peptide (Mut11–PBSE) in Phase I. (a) RMSD profile over 10 ns. (b) Radius of gyration (R_g) analysis.

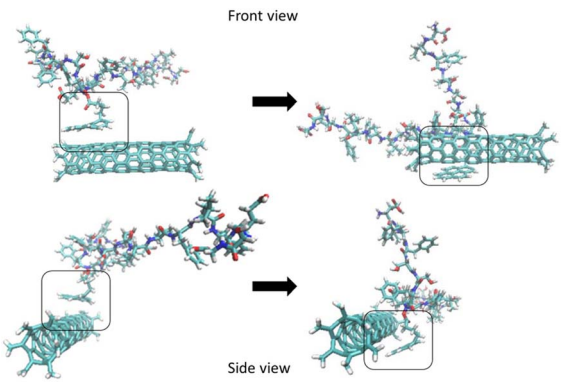

Fig. 13 Conformational shift of the pyrene group during molecular dynamics simulation in Phase II. Structural visualization of the conjugated peptide with a single-walled carbon nanotube (SWCNT) substrate showing the orientation change of the pyrene moiety. Top row: Front view before (left) and after (right) simulation. Bottom row: Side view before (left) and after (right) simulation. The boxed areas highlight the repositioning of the pyrene group as it interacts more closely with the SWCNT surface over the course of the simulation.

less folded, reflecting its state before molecular dynamics and interaction with SWCNT. After 10 ns, the peptide shows increased folding and a more organized structural arrangement around the SWCNT, indicating a more stable conformation. Additionally, the movement of the pyrene group from PBSE is observed, shifting from above the SWCNT (black box) to below it by the end of the simulation, suggesting significant interaction between PBSE and SWCNT.

Fig. 14a shows that RMSD in Phase II fluctuated significantly during the first 2 ns, then stabilized for the remainder of the 10 ns simulation. The average RMSD was 2.703 nm with a standard deviation of 0.844 nm. This value is approximately four times higher than the average RMSD in Phase I. The increase indicates greater conformational changes in the peptide structure during interaction with SWCNT. This increase reflects the dynamic interaction between the peptide and CNT surface. The higher fluctuation is consistent with Badhe *et al.* (2021),[42] who observed a 3 to 4 times increase in RMSD for peptide and SWCNT complexes in phase II.

Fig. 14b shows the radius of gyration (R_g) of phase II simulation ranged from 1.0 to 1.4 nm, with initial fluctuations up to 3000 ps, followed by stable values. The average R_g was 1.211 nm with a standard deviation of 0.115 nm, indicating a compact structure with minimal variation. Compared to Phase I, the R_g decreased by 13.1%, suggesting that SWCNT contributes to a more compact peptide conformation. Similar R_g reductions were also reported by Martí *et al.* (2022)[44] in antibody–substrate systems. In their study, the interaction between antibodies and solid substrates such as gold and silica led to a noticeable decrease in R_g (about 8%), reflecting enhanced structural

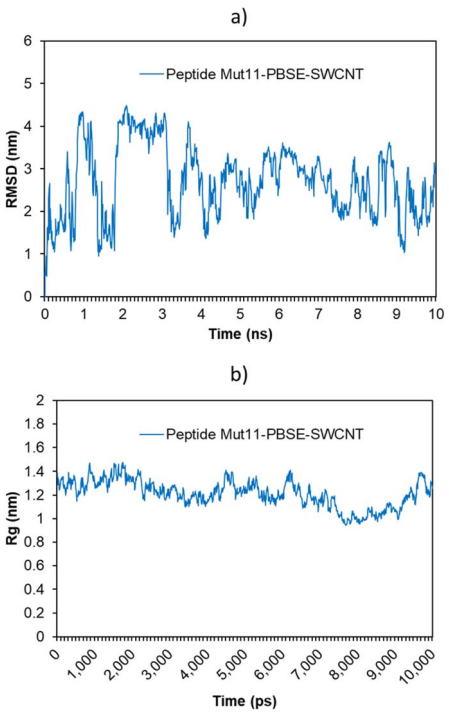

Fig. 14 Molecular dynamic result (a) RMSD, and (b) radius gyration of peptide Mut11-PBSE at surface of SWCNT in Phase II.

compactness. Overall, the SWCNT substrate combined with the PBSE linker demonstrated strong potential for future NS1 DENV-2 detection systems, with Mutant peptide 11 serving as the key sensing element.

4. Discussion

Dengue virus (DENV) nonstructural protein 1 (NS1) has emerged as a critical factor in viral pathogenesis, contributing to multiple aspects of infection and disease progression. Research has revealed that NS1 can reach concentrations up to 50 μg mL^{-1} in patient during acute infection, making it both a valuable diagnostic marker and a significant pathogenic determinant.[45] Interestingly, NS1 exhibits structural and functional similarities to host high-density lipoprotein (HDL), which may contribute to its pathogenic capabilities. This molecular mimicry potentially allows NS1 to interact with host systems in ways that promote viral survival and disease progression, blurring the lines between self and non-self recognition by the immune system.[46]

Peptide-based biosensors offer several advantages for viral detection, including high specificity, stability, ease of synthesis, and adaptability to various sensor platforms. Although peptide-based biosensors have shown promise for the detection of DENV-2 through specific interactions with the NS1 protein, only a limited number of studies have explored this approach in detail. For instance, a synthetic peptide (DGV BP1) identified *via* phage display was reported to bind specifically to DENV-2 NS1 with a detection limit of approximately 1.49 μg mL^{-1}.[23] Another study demonstrated that peptides with strong binding affinity could be immobilized onto electrochemical sensor platforms, enabling sensitive and serotype-specific detection of DENV-2 NS1.[22] However, the sequence of the NS1 protein exhibits significant variability depending on the geographic origin of the virus. This study aims to address this limitation by designing and characterizing a peptide with enhanced binding affinity specifically toward the NS1 protein of DENV-2 isolates from Indonesia.

Therefore, the initial step of this study involved screening representative NS1 gene sequences of DENV-2 from Indonesia through phylogenetic and mutation analyses using data from the GenBank database (NCBI). Constructing a phylogenetic tree allows us to identify evolutionary relationships among different NS1 sequences. Sequences located at the outer clades with fewer mutations are often considered more conserved and less mutations represent a lower rate of genetic change.[47] Based on this analysis, the NS1 sequence AHK09925.1 was selected as a representative Indonesian strain and subsequently used for 3D structural modelling using a homology modelling approach.

Homology modelling with the trRosetta web server combines deep learning-based inter-residue geometry prediction with Rosetta's energy minimization framework to generate accurate protein structure models.[25] TM-score quantifies the structural similarity between predicted and reference protein models, *E*-value assesses the statistical significance of sequence-template matches, and *Z*-score evaluates how exceptional a model or alignment score is compared to random background. These metrics collectively guide the reliability and accuracy of homology modeling in trRosetta.[48]

In this study, the NS1 DENV-2 model showed a high TM-score (0.948), low *E*-value, and high *Z*-score, indicating a reliable structure composed of α-helices, β-sheets, and loops, characteristic of the native NS1 protein. Furthermore, Ramachandran analysis revealed this protein has high-quality protein models 91.6% of residues within favored regions and no residues in disallowed regions, reflecting physically plausible backbone geometry and reliable structural integrity.[49]

One effective approach to peptide design, as described in our previous study by Jauhar *et al.* (2024)[27] and also supported by Mastouri *et al.* (2022),[20] involves identifying peptide sequences based on the binding interface of receptor or antibody complexes. This method targets interface residues located within approximately 4 Å of the peptide and uses computational tools to optimize interactions at these sites. Notably, it accounts for the flexibility of both the receptor and the peptide by modeling conformational ensembles rather than assuming a rigid structure.[20,50]

Since the modeled 3D structure of the Indonesian NS1 DENV-2 protein lacked a defined antibody-binding interface, we searched for a highly similar structure with known antibody interactions in the Protein Data Bank (PDB). Using the BLASTp webserver, we identified PDB ID: 7BSC (Chain A), which shares 99% sequence identity with the Indonesian NS1 DENV-2 sequence. The peptide was designed based on the binding residues at the active site of 7BSC in complex with the heavy and light chains of the antibody. The 3D structure of the designed peptide was then predicted using the trRosetta web server, and its stereochemical quality was validated through Ramachandran plot analysis. As a result, the unmutated peptide has 100% of residues in the most favorable regions and achieved an ERRAT score of 100. Although TM-Score has lower score of 0.177, this was above the statistical noise threshold (>0.170) which means it corresponds to a *P*-value slightly below 1, indicating 2% chance of occurring randomly, since 98% of random pairs score $\leq$0.17.[48,51]

Furthermore, peptide mutations were introduced through sequential single-point substitutions: glycine was replaced with leucine or tyrosine, tyrosine with lysine or glutamic acid, and serine with tryptophan. Among the 13 peptide variants generated, Mutants 10, 11, and 13 exhibited the most favorable binding characteristics, as evidenced by their highest HADDOCK scores and lowest binding free energy values when docked with the NS1 DENV-2 receptor from the Indonesian strain. These three mutants consistently outperformed the others in binding affinity and stability predictions.

Mutant 10 contains two-point mutations: tyrosine at position 8 (Y8) is replaced with lysine (K), and serine at position 19 (S19) is replaced with tryptophan (W). The Y8 → K substitution shifts the interaction potential from hydrophobic and aromatic to electrostatic dominance. Although Y8 does not interact with any residues in the unmutated peptide, its substitution with lysine introduces a positively charged side chain capable of forming ionic interactions with negatively charged residues.[52] This was confirmed with by interaction analysis, which showed that Lys8

formed new salt bridges with Gly292 on the target protein (Fig. 15a).

Mutant 11 involves two-point mutations: glycine at position 3 is replace with tyrosine (Y), and tyrosine at position 8 (Y8) is substituted with glutamic acid (E). Glycine, being the smallest amino acid and lacking a side chain, contributes minimally to binding interactions. Replacing it with tyrosine introduces an aromatic ring and a hydroxyl group, can enhance hydrophobic interactions, enabling hydrogen bonding, and facilitating π–π stacking.[53]

As shown in Fig. 15b, Tyr 3 forms a new hydrogen bond with Asn246 and enhances salt bridge formations with Ala352, Thr264 and Thr351. Meanwhile, the Y8 → E mutation introduces a negatively charge side chain, enabling ionic interactions with positively charges residues on the protein target. Additionally, glutamic acid's smaller side chain compared to tyrosine's bulky aromatic ring may reduce steric hindrance, allowing the peptide backbone to adopt more favorable conformations.[54] This is consistent with the docking result, which showed that Mut-11 formed more interactions, specifically, increasing from 7 to 11 hydrogen bonds and from 149 to 152 van der Waals contacts.

Mut-13 includes two substitutions: tyrosine is replaced with glutamic acid, and serine is replaced with tryptophan. Glutamic acid carries a negatively charged side chain at physiological pH, allowing it to form ionic or salt–bridge interactions with positively charged residues on the target surface. While tyrosine's aromatic ring and hydroxyl group contribute to hydrophobic and hydrogen bonding, glutamic acid can form multiple hydrogen bonds and ionic interactions, which may stabilize different peptide conformations and improve binding thermodynamics.[55] This is supported by docking analysis that Glu8 formed new hydrogen bond and salt bridge with Lys341 (Fig. 15c).

Meanwhile, the S19 → W substitution introduces a bulky indole ring, which enhances hydrophobic contacts and facilitates π–π stacking with aromatic or hydrophobic residues on the target protein. Compared to serine, which contains only a small hydroxyl group, tryptophan contributes significantly to peptide-target stabilization by occupying hydrophobic pockets, reducing conformational flexibility, and increasing van der Waals contacts.[56] This is further supported by docking interaction analysis, which confirmed that Trp19 increased the number of salt bridges to seven, involving residues such as Asn347, Val346, Glu343, Leu345, Asn344, and Leu349.

Furthermore, molecular dynamics (MD) simulation analysis demonstrated that the NS1 DENV-2 complex with Mut-11 exhibited the most stable conformation, as indicated by the lowest average RMSD value of 0.273 nm, outperforming all other mutant complexes as well as the unmutated peptide. Interaction dynamics over the 25 ns simulations of all complexes were also assessed (Table 6). The Mut-13 complex showed the greatest loss of hydrogen bonds with the target protein, followed by the Mut-10 complex. A similar trend was observed in the number of van der Waals interactions, suggesting a reduction in binding stability for these mutants throughout the simulation period. In contrast, Mut-11 maintained four strong hydrogen bonds out of the initial eight until the end of the simulation, with the addition of one new salt bridge, further contributing to its enhanced binding stability.

Selectivity study of peptide mut-11 through interactions with four different NS1 proteins evaluated through molecular docking and dynamics simulations. The structural dynamics analysis of peptide Mut-11 in complex with flaviviral NS1 proteins provides critical insights into its selective binding behavior and potential as a dengue-specific targeting agent. The RMSD analysis and structural visualization revealed that Mut-11 maintains a stable and compact conformation when bound to DENV-2, DENV-3, and DENV-4 NS1 proteins, while displaying greater fluctuations and loss of binding stability with DENV-1 and ZIKV.

This stability in DENV-2, -3, and -4 complexes, indicated by lower RMSD values and consistent structural integrity over 25 ns of simulation, points to favorable interaction energetics and structural complementarity. Notably, the DENV-2 complex showed the most pronounced binding stability, aligning with its superior binding free energy ($\Delta G = -12.5$ kJ mol^{-1}) and strongest predicted affinity ($K_d = 7.2 \times 10^{-10}$ M). In contrast, the significantly higher RMSD observed in the DENV-1 complex, reaching up to 1 nm, reflects a weaker and more dynamic interaction, possibly driven by steric mismatch or unfavorable electrostatic contacts. This instability was also evident in the ZIKV complex, which demonstrated partial detachment of the peptide after 10 ns, suggesting transient interactions and limited compatibility.

As shown in Fig. S5 and Table S3, the interaction profiles of the peptide varied across DENV and ZIKV NS1 complexes during

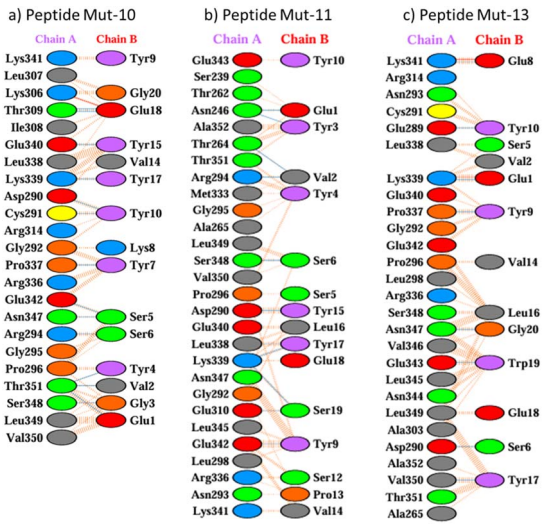

Fig. 15 Molecular interaction profiles of peptide Mutants (Chain B) with NS1 DENV-2 protein (Chain A). Schematic representation of the residue-level interactions between NS1 DENV-2 and three peptide mutants: (a) peptide Mut-10, (b) peptide Mut-11, and (c) peptide Mut-13. Each panel illustrates non-bonded contacts (orange dashed lines), hydrogen bonds (blue lines), and salt bridges (red lines) between specific residues from Chain A (NS1) and Chain B (peptide mutants). The Fig. highlights how mutations affect binding interface and interaction strength, offering insights into the binding affinity and specificity of each mutant.

Table 6 Hydrogen bond and van der Waals interactions of peptide mutants with NS1 DENV-2 during molecular dynamic simulations

	Initial simulation ($t = 0$ ns)			Final simulation ($t = 25$ ns)		
System	Residue (NS1 – Peptida)	Distance (Å)	Non-bonded contact	Residue (NS1 – Peptida)	Distance (Å)	Non-bonded contact
Peptide Mut 10-CNT	GLY292 – LYS8	3.12	109	ASP290 – SER12	2.93	42
	ARG294 – SER6	2.91		GLY292 –TYR15	2.85	
	THR309 –GLU18	2.71		ASN293 –TYR10	3.20	
	THR309 –GLU18	2.65		GLU340 – TRP15	3.23	
	LYS339 – TYR17	2.73				
	GLU340 –TYR15	2.78				
	GLU342 – SER5	2.54				
	THR351 – GLU1	2.79				
	THR351 – VAL2	2.79				
Peptide Mut 11-CNT	SER239 – GLU1	2.94	88	LYS245 – GLU1	2.85	46
	THR264 – VAL2	2.79			3.12	
	ASP290 – TYR15	2.67		LYS245 – GLU1	2.95	
	GLU310 – SER19	2.84			2.98	
	LEU338 –TYR17	3.01		THR264 – TYR3	2.32	
	LYS339 – TYR17	2.94		ASN293 – SER12		
	LYS339 – SER19	2.89				
	GLU342 – TYR9	2.55		LYS339 – SER19		
Peptide Mut 13-CNT	GLU289 –TYR10	2.79	93	LEU349 – TRP19	3.17	32
	ASP290 – SER6	2.71		THR351 –GLU18	2.61	
	LYS339 – GLU1	2.81				
	GLU340 – TYR9	2.68				
	LYS341 – GLU8	2.75				
	GLU343 – TRP19	2.67				
	ASN347 –GLY20	3.21				
	VAL350 –TYR17	3.31				

the 25 ns MD simulations. For DENV-2, hydrogen bonds were maintained consistently (8 at the initial frame, 4 at the midpoint, and 5 at the final frame), accompanied by stable non-bonded contacts (45–46). This indicates a sustained and stable binding mode with DENV-2 NS1. In contrast, ZIKV NS1 exhibited a marked reduction in interactions, with hydrogen bonds decreasing from 8 to 4 and non-bonded contacts dropping from 74 to 41, reflecting weaker and less stable binding. Among the other serotypes, DENV-1 showed a drastic loss of hydrogen bonds from 9 to zero and non-bonded contacts (from 102 initially to only 2 at the midpoint), suggesting partial detachment of the peptide before partial recovery at the final frame. DENV-3 and DENV-4 maintained relatively stable interactions of hydrogen bonds and non-bonded contacts remaining steady throughout the simulation. These findings collectively indicate that the designed peptide achieves stable and selective binding with DENV-2, DENV-3 and DENV4 NS1, while interactions with and ZIKV significantly weaker, thereby supporting the peptide's potential as a specific bioreceptor for dengue virus detection.

The specificity of peptide Mut-11 can be attributed, in part, to the high sequence and structural conservation among the NS1 proteins of DENV serotypes, particularly DENV-2, -3, and -4. This evolutionary relatedness appears to facilitate optimal interaction surfaces, as opposed to the more divergent NS1 of ZIKV, which shares only partial homology. From a functional perspective, this selective binding profile is highly desirable for developing peptide-based diagnostics that minimize cross-reactivity with other flaviviruses.

To explore the potential application of peptide mutations for the detection of NS1 DENV-2, this study employed *in silico* design to predict the ability of the Mut-11 peptide to functionalize sensor substrates effectively.[57] Among various carbon-based nanomaterials, carbon nanotubes (CNTs)—particularly single-walled carbon nanotubes (SWCNTs)—have emerged as highly promising platforms for electrochemical biosensing due to their exceptional electrical conductivity, high current mobility, thermal stability, and nanoscale diameter.[58]

Peptide-CNT thin-film transistors (TFTs) have demonstrated sequence-independent nucleic acid detection through electrostatic interactions. For example, a decapeptide functionalized with pyrene groups was shown to adsorb onto CNTs *via* π–π stacking, enabling sensitive RNA/DNA detection by modulating device conductivity.[59] Similarly, Fernández-Sánchez *et al.* covalently immobilized a chimeric fibrin–filaggrin peptide (CFFCP1) on carboxylated multi-walled CNTs (MWCNTs) *via* EDC–NHS coupling chemistry, enabling the selective detection of anti-CFFCP1 antibodies in both rabbit and human sera, with minimal response from healthy controls—demonstrating the high specificity of the peptide-functionalized sensor.[21]

A critical aspect in designing peptide-functionalized SWCNT systems lies in preserving the biological activity of the peptide while achieving stable conjugation. This requires a detailed understanding of the interaction forces, such as hydrophobic,

electrostatic, and π–π interactions, that govern peptide–SWCNT interfaces.[60]

However, the challenge is conjugating peptide on the surface of SWCNT with covalent bondings, can ruin the electronic behavior of SWCNT and even functionalization perturbs and even diminishes SWCNT optical properties. Therefore, conjugating with non-covalent methods allows peptide immobilization on the surface of SWCNT with biocharacterization capabilities by altering the extended π-conjugated system of the nanotube, one of which using linker molecules.

Most of the ways to attach proteins or peptides to SWCNTs without damaging them fall into two main categories. First, adsorptive methods, where proteins simply stick to the nanotube surface. Second, Hybrid method switch use both sticking and a gentle chemical link (*e.g.*, using a molecule like PBSE).[61] Previously, Badhe *et al.* (2021)[42] reported that peptide immobilization on CNT surfaces can be effectively achieved using 1-pyrenebutanoic acid succinimidyl ester (PBSE) as a bifunctional linker. PBSE offers strong non-covalent π–π stacking between its pyrene moiety and the graphitic CNT surface, while its succinimidyl ester group forms stable covalent bonds with amine groups on peptides, ensuring robust and functional attachment.

In this context, our study investigated the potential of the optimized Mut-11 peptide to interact with SWCNT surfaces using *in silico* modelling (molecular dynamic approach), offering insights into its applicability as a bio-recognition element in next-generation NS1 DENV-2 biosensors.

Molecular dynamics (MD) simulations were conducted in two stages. First, the Mut-11 peptide was conjugated with PBSE and structurally optimized. In the second stage, the behavior of the Mut-11–PBSE complex on a SWCNT surface was evaluated over a 10 ns simulation. As shown in Fig. 13, the final structure demonstrated stable anchoring of the PBSE linker to the SWCNT surface, facilitated by strong π–π stacking interactions between the pyrene moiety and the graphitic structure of the SWCNT. The interaction between the conjugated peptide and SWCNT in Phase II was assessed by measuring the distance between the pyrene moiety's center of mass and the SWCNT surface. The pyrene group in PBSE interacts with SWCNT primarily through π–π stacking. As shown in Fig. 16a, this distance fluctuates throughout the simulation, reflecting the dynamic adjustment of pyrene to maximize its interaction. By the end of the 10 ns run, the pyrene–SWCNT separation stabilized at 0.8 nm, which is greater than the 0.36 nm optimal distance reported by Cai *et al.* (2016).[62] This discrepancy is likely due to the smaller-diameter CNTs used here, whose sharper curvature alters pyrene orientation and reduces stacking efficiency.

To further understand the interaction, a Surface Radial Distribution Function (sRDF) analysis was performed to examine how particles are distributed on the SWCNT surface. The sRDF for the pyrene group relative to SWCNT, as shown in Fig. 16b, peaks at 0.84 nm with an sRDF value of 40, indicating a strong and stable interaction at this distance. This peak aligns with the final distance observed in the previous distance analysis, confirming consistent interaction patterns. The alignment

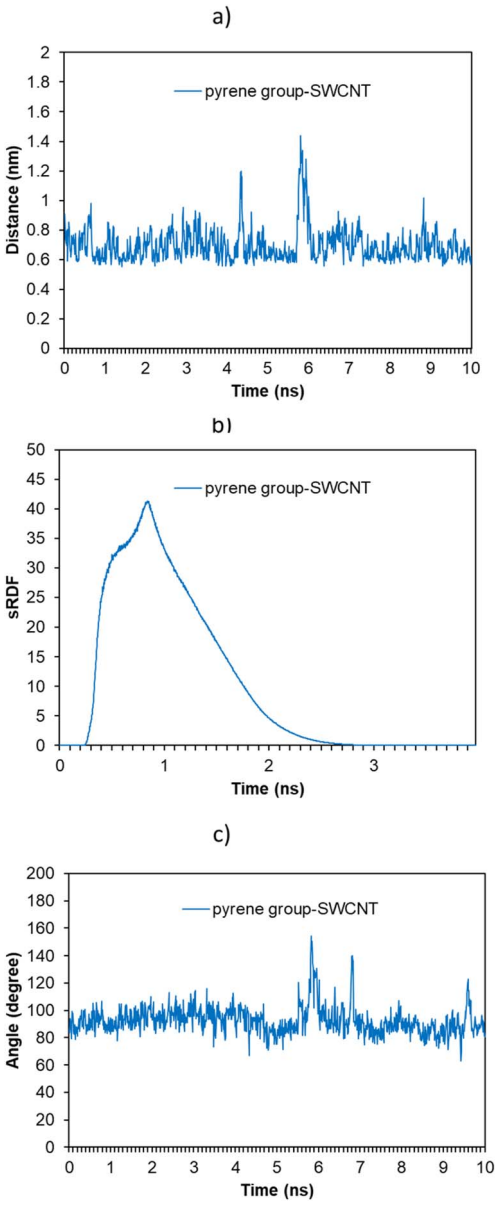

Fig. 16 Molecular dynamics evaluation of pyrene group interaction with SWCNT surface in PBSE-Mut11 peptide conjugate. (a) Distance profile showing the variation in the center-of-mass distance between the pyrene group and SWCNT surface over a 10 ns simulation. (b) Radial distribution function (sRDF) indicating the probability density of the pyrene group relative to the SWCNT surface. (c) Angular distribution analysis revealing the orientation fluctuation (in degrees) of the pyrene group with respect to the SWCNT surface over time. These analyses collectively illustrate the dynamic adsorption behavior and structural stability of the conjugate system.

of this peak with the final distance observed further supports the importance of considering SWCNT curvature in optimizing these interactions, as the curvature can significantly impact the stability and effectiveness of π–π stacking interactions.

Additionally, angular analysis of the pyrene group's orientation relative to SWCNT provides insights into molecular alignment and stability. Fig. 16c shows significant fluctuations in the angle between the pyrene group and SWCNT throughout

the simulation. Initially, the angle is stable at around 100°, indicating steady alignment. However, between 70 and 90 ns, the angle shifts significantly, reflecting dynamic adjustments. Eventually, the angle stabilizes at 92.3°, suggesting a nearly parallel orientation to the SWCNT surface. This parallel orientation optimizes π–π interactions, crucial for molecular binding and stability. This observed angle aligns with similar studies, where it was reported a similar final angle of 88.6°, confirming the energetic stability of this alignment and its role in enhancing molecular system stability.

Several recent *in silico* studies have proposed peptides for viral antigen recognition and examined peptide behavior on carbon-based surfaces. For example, Badhe *et al.* (2021) combined molecular dynamics and PMF calculations to design peptides for the SARS-CoV-2 RBD and assessed peptide interactions with functionalized graphene/CNT surfaces,[42] while Mastouri *et al.* (2022) applied structure-guided extraction of binding regions from protein–protein interfaces followed by point mutations and *in silico* validation (docking and MD).[20] Our approach differs in three key aspects. First, the target antigen is DENV-2 NS1 from Indonesia. Second, whereas prior work typically focused on either peptide–antigen binding or peptide–carbon adsorption in isolation, we simultaneously optimize peptide sequences for both antigen affinity and integration with functionalized SWCNT scaffolds, producing a dual-level design optimized for biosensor implementation. Third, our peptide candidates are derived *via* epitope mapping and rational mutagenesis guided by the PDB structures most closely related to Indonesian DENV-2 isolates, grounding the designs in strain-relevant structural features.

We acknowledge that this study is purely computational. Nevertheless, our *in silico* framework provides an alternative strategy for designing peptides specific to DENV-2 NS1. Studies by Songprakhon *et al.* 2020; Lim *et al.* 2018 and Kim *et al.* 2019 employed biopanning (an affinity-based phage-display selection technique that uses iterative rounds of binding, washing, elution, and amplification) to experimentally enrich peptides that bind tightly and specifically to dengue virus NS1.[22,23,40] In contrast, our computational study reproduces the key elements of biopanning through an *in silico* workflow of structure-guided extraction of binding regions from protein–protein interfaces. As Min *et al.* (2024) classify,[63] computational peptide-design methods fall into three broad categories: molecular dynamics, *de novo* design, and machine-learning approaches. Our methodologies primarily leverage molecular-dynamics-based and structure-guided design, with the potential to integrate machine-learning strategies in future work.

Although the presented computational framework provides strong evidence for the stability, selectivity, and compatibility of the designed peptide bioreceptor with SWCNT transducer surfaces, this study is limited by the lack of wet-lab validation. Experimental assays such as surface plasmon resonance (SPR), isothermal titration calorimetry (ITC), or cell-based assays could confirm binding affinities and specificities under physiological conditions. Furthermore, prototype biosensor fabrication followed by performance testing would be necessary to validate the computational predictions. These future studies will provide the crucial link between *in silico* predictions and translational biosensor applications.

5. Conclusions

The integrative *in silico* framework presented here offers a comprehensive approach to peptide screening by combining phylogenetic analysis, protein and peptide modeling, molecular docking, and dynamic simulations to explore potential peptide mutations and their interactions with NS1 proteins, as well as nanomaterial conjugation. The analysis suggests that Mut-11 may represent a relatively stable and high-affinity candidate for NS1 DENV-2, showing potential specificity for detecting NS1 proteins of dengue virus (DENV-2, DENV-3, and DENV-4, but not DENV-1) over ZIKA virus. Preliminary evaluation also indicates possible compatibility with carbon nanotube-based transducer surfaces without substantially affecting their optoelectronic properties. However, this study is limited by the absence of experimental validation. Future *in vitro* experiments, including peptide–protein interaction assays and biosensor prototype testing, will be critical to confirm the computational findings and advance the designed peptide bioreceptor toward practical diagnostic applications.

Author contributions

PHS: conceptualization, methodology, data curation, and writing – original draft preparation; SAP: methodology and data curation; FA: methodology and data curation; MMJ: conceptualization, methodology and writing – original draft preparation; MFRW: data curation and writing – original draft preparation; DWCN: data curation; AA: data curation; EM: resources and supervision; RS: funding acquisition; YW: funding acquisition; IA: writing – review and editing, resources, supervision, and funding acquisition. All authors have read and agreed to the published version of the manuscript.

Conflicts of interest

There are no conflicts to declare.

Data availability

The authors confirm that the data supporting the findings of this study are available as part of the supplementary information (SI). Supplementary information: Table S1: NS1 DENV-2 gene data from diverse geographical regions across Indonesia. Table S2: 3D structural modelling of peptide mutants and Ramachandran plot analysis. Fig. S1: Phylogenetic trees of Indonesian dengue virus NS1 protein sequences. Fig. S2: RMSF of peptide Mut-11 in complex with NS1 proteins of DENV-1, DENV-3, DENV-4, and ZIKV. Table S3: Total interactions of peptides with DENV and ZIKV during MD simulations. Fig. S3: Radius of gyration (R_g) profiles of Mut-11 peptide in complex with NS1 proteins from different flaviviruses during 25 ns molecular dynamics (MD) simulations. Fig. S4: Radius of gyration (R_g) profiles of Mut-11 peptide in complex with NS1

proteins from different flaviviruses during 25 ns molecular dynamics (MD) simulations. Fig. S5: Molecular interaction profiles of peptide mutants (chain B) with (a) DENV-1, (b) DENV-3, (c) DENV-4, (d) ZIKV. See DOI: https://doi.org/10.1039/d5ra04799d.

Acknowledgements

The authors thank Institut Teknologi Bandung for research grant Riset Kolaborasi Indonesia Skema C Tahun 2025 [Contract No. 1389/IT1.B07.1/TA.00/2025] for supporting this research. This work also supported by Institut Teknologi Bandung through Riset Unggulan ITB 2025 program [Contract No. 841/IT1.B07.1/TA.00/2025]. In addition, the authors are grateful for the research facilities provided by Nano Center Indonesia.

References

1 P. S. Indu, T. S. Anish, S. Chintha, G. K. Libu, L. Tony, N. S. Siju, E. Sreekumar, A. Santhoshkumar, R. Aravind, K. L. Saradadevi, S. Sunija, J. Johnson, M. G. Anupriya, T. Mathew, K. J. Reena, V. Meenakshy, P. Namitha, N. P. Kumar, R. Kumari, A. J. Mohamed, B. Nagpal, S. Sarkar, R. Sadanandan and R. Velayudhan, *Lancet Reg. Health Southeast Asia*, 2024, **22**, 100337.
2 S.-X. Zhang, G.-B. Yang, R.-J. Zhang, J.-X. Zheng, J. Yang, S. Lv, L. Duan, L.-G. Tian, M.-X. Chen and Q. Liu, *Decoding Infect. Transm.*, 2024, **2**, 100021.
3 R. F. do Carmo, J. V. J. Silva Júnior, A. F. Pastor and C. D. F. de Souza, *Infect. Dis. Poverty*, 2020, **9**, 1–16.
4 L. Li, X. Guo, X. Zhang, L. Zhao, L. Li, Y. Wang, T. Xie, Q. Yin, Q. Jing and T. Hu, *Infect. Dis. Poverty*, 2022, **11**, 107.
5 B. Sierra, A. C. Magalhães, D. Soares, B. Cavadas, A. B. Perez, M. Alvarez, E. Aguirre, C. Bracho, L. Pereira and M. G. Guzman, *Viruses*, 2021, **13**, 1540.
6 J. P. Messina, O. J. Brady, T. W. Scott, C. Zou, D. M. Pigott, K. A. Duda, S. Bhatt, L. Katzelnick, R. E. Howes and K. E. Battle, *Trends Microbiol.*, 2014, **22**, 138–146.
7 S. P. Yenamandra, C. Koo, S. Chiang, H. S. J. Lim, Z. Y. Yeo, L. C. Ng and H. C. Hapuarachchi, *Sci. Rep.*, 2021, **11**, 13496.
8 S. Halstead, *F1000Research*, 2019, **8**, F1000–Faculty.
9 C. Guo, Z. Zhou, Z. Wen, Y. Liu, C. Zeng, D. Xiao, M. Ou, Y. Han, S. Huang and D. Liu, *Front. Cell. Infect. Microbiol.*, 2017, **7**, 317.
10 R. Aguas, I. Dorigatti, L. Coudeville, C. Luxemburger and N. M. Ferguson, *Sci. Rep.*, 2019, **9**, 9395.
11 J. R. Fried, R. V Gibbons, S. Kalayanarooj, S. J. Thomas, A. Srikiatkhachorn, I.-K. Yoon, R. G. Jarman, S. Green, A. L. Rothman and D. A. T. Cummings, *PLoS Neglected Trop. Dis.*, 2010, **4**, e617.
12 R. T. Sasmono, A.-F. Taurel, A. Prayitno, H. Sitompul, B. Yohan, R. F. Hayati, A. Bouckenooghe, S. R. Hadinegoro and J. Nealon, *PLoS Neglected Trop. Dis.*, 2018, **12**, e0006616.
13 M. R. Hasan, P. Sharma, S. Khan, U. M. Naikoo, K. Bhalla, M. Z. Abdin, N. Malhotra, T. M. Aminabhavi, N. P. Shetti and J. Narang, *Sens. Diagn.*, 2025, **4**, 7–23.
14 H. B. Y. Chan, C. H. How and C. W. M. Ng, *Singapore Med. J.*, 2017, **58**, 632.
15 B. Coleman, C. Coarsey, M. A. Kabir and W. Asghar, *Sens. Actuators, B*, 2019, **282**, 225–231.
16 M. A. Kabir, H. Zilouchian, M. Sher and W. Asghar, *Diagnostics*, 2020, **10**, 42.
17 S. Alcon, A. Talarmin, M. Debruyne, A. Falconar, V. Deubel and M. Flamand, *J. Clin. Microbiol.*, 2002, **40**, 376–381.
18 A. Aryati, H. Trimarsanto, B. Yohan, P. Wardhani, S. Fahri and R. T. Sasmono, *BMC Infect. Dis.*, 2013, **13**, 1–11.
19 X. Xiao, Z. Kuang, J. M. Slocik, S. Tadepalli, M. Brothers, S. Kim, P. A. Mirau, C. Butkus, B. L. Farmer and S. Singamaneni, *ACS Sens.*, 2018, **3**, 1024–1031.
20 M. Mastouri, S. Baachaoui, A. Mosbah and N. Raouafi, *RSC Adv.*, 2022, **12**, 13003–13013.
21 M. de Gracia Villa, C. Jiménez-Jorquera, I. Haro, M. J. Gomara, R. Sanmartí, C. Fernández-Sánchez and E. Mendoza, *Biosens. Bioelectron.*, 2011, **27**, 113–118.
22 J. M. Lim, J. H. Kim, M. Y. Ryu, C. H. Cho, T. J. Park and J. P. Park, *Anal. Chim. Acta*, 2018, **1026**, 109–116.
23 J. H. Kim, C. H. Cho, M. Y. Ryu, J.-G. Kim, S.-J. Lee, T. J. Park and J. P. Park, *PLoS One*, 2019, **14**, e0222144.
24 K. Tamura, G. Stecher and S. Kumar, *Mol. Biol. Evol.*, 2021, **38**, 3022–3027.
25 Z. Du, H. Su, W. Wang, L. Ye, H. Wei, Z. Peng, I. Anishchenko, D. Baker and J. Yang, *Nat. Protoc.*, 2021, **16**, 5634–5651.
26 C. Colovos and T. O. Yeates, *Protein Sci.*, 1993, **2**, 1511–1519.
27 M. M. Jauhar, F. R. Damairetha, E. Mardliyati, M. F. Ulum, P. H. Syaifie, F. Fahmi, A. Satriawan, W. Shalannanda and I. Anshori, *PLoS One*, 2024, **19**, e0305770.
28 M. Johnson, I. Zaretskaya, Y. Raytselis, Y. Merezhuk, S. McGinnis and T. L. Madden, *Nucleic Acids Res.*, 2008, **36**, W5–W9.
29 Schrödinger LLC, The PyMOL Molecular Graphics System, Version∼1.8, 2015.
30 G. C. P. van Zundert, J. P. G. L. M. Rodrigues, M. Trellet, C. Schmitz, P. L. Kastritis, E. Karaca, A. S. J. Melquiond, M. van Dijk, S. J. de Vries and A. M. J. J. Bonvin, *J. Mol. Biol.*, 2016, **428**, 720–725.
31 C. Dominguez, R. Boelens and A. M. J. J. Bonvin, *J. Am. Chem. Soc.*, 2003, **125**, 1731–1737.
32 L. C. Xue, J. P. Rodrigues, P. L. Kastritis, A. M. Bonvin and A. Vangone, *Bioinformatics*, 2016, **32**, 3676–3678.
33 A. Vangone and A. M. J. J. Bonvin, *Elife*, 2015, **4**, e07454.
34 R. A. Laskowski, *Protein Sci.*, 2022, **31**, e4473.
35 K. Mahnam, M. Lotfi and F. A. Shapoorabadi, *J. Mol. Graphics Modell.*, 2021, **107**, 107952.
36 Z. Ghobadi, K. Mahnam and M. Shakhsi-Niaei, *J. Mol. Graphics Modell.*, 2022, **111**, 108079.
37 M. J. Abraham, T. Murtola, R. Schulz, S. Páll, J. C. Smith, B. Hess and E. Lindahl, *SoftwareX*, 2015, **1–2**, 19–25.
38 B. R. Brooks, C. L. Brooks III, A. D. Mackerell Jr, L. Nilsson, R. J. Petrella, B. Roux, Y. Won, G. Archontis, C. Bartels and S. Boresch, *J. Comput. Chem.*, 2009, **30**, 1545–1614.
39 W. Huang, Z. Lin and W. F. van Gunsteren, *J. Chem. Theory Comput.*, 2011, **7**, 1237–1243.

40 P. Songprakhon, T. Thaingtamtanha, T. Limjindaporn, C. Puttikhunt, C. Srisawat, P. Luangaram, T. Dechtawewat, C. Uthaipibull, S. Thongsima, P. Yenchitsomanus, P. Malasit and S. Noisakran, *Sci. Rep.*, 2020, **10**, 12933.
41 N. Modhiran, D. Watterson, D. A. Muller, A. K. Panetta, D. P. Sester, L. Liu, D. A. Hume, K. J. Stacey and P. R. Young, *Sci. Transl. Med.*, 2015, **7**, 304ra142.
42 Y. Badhe, R. Gupta and B. Rai, *RSC Adv.*, 2021, **11**, 3816–3826.
43 P. Mark and L. Nilsson, *J. Phys. Chem. B*, 2002, **106**, 9440–9445.
44 D. Martí, E. Martín-Martínez, J. Torras, O. Betran, P. Turon and C. Alemán, *Colloids Surf., B*, 2022, **213**, 112400.
45 H.-R. Chen, Y.-C. Lai and T.-M. Yeh, *J. Biomed. Sci.*, 2018, **25**, 58.
46 A. C. Alcalá and J. E. Ludert, *PLoS Pathog.*, 2023, **19**, e1011587.
47 R. Zhao, A. Talenti, L. Fang, S. Liu, G. Liu, N. P. Chue Hong, A. Tenesa, M. Hassan and J. G. D. Prendergast, *Commun. Biol.*, 2022, **5**, 1003.
48 J. Xu and Y. Zhang, *Bioinformatics*, 2010, **26**, 889–895.
49 A. Wlodawer, *Methods Mol. Biol.*, 2017, **1607**, 595–610.
50 P. A. Valiente, H. Wen, S. Nim, J. Lee, H. J. Kim, J. Kim, A. Perez-Riba, Y. P. Paudel, I. Hwang, K.-D. Kim, S. Kim and P. M. Kim, *J. Med. Chem.*, 2021, **64**, 14955–14967.
51 Y. Zhang and J. Skolnick, *Proteins: Struct., Funct., Bioinf.*, 2004, **57**, 702–710.
52 H. Teimouri, Z. S. Ghoreyshi, A. B. Kolomeisky and J. T. George, *Front. Immunol.*, 2025, **15**, 1510435.
53 D. W. Sammond, Z. M. Eletr, C. Purbeck, R. J. Kimple, D. P. Siderovski and B. Kuhlman, *J. Mol. Biol.*, 2007, **371**, 1392–1404.
54 M. J. Moore, J. A. Adams and S. S. Taylor, *J. Biol. Chem.*, 2003, **278**, 10613–10618.
55 E. R. Unanue, *J. Immunol.*, 2011, **186**, 7–8.
56 Y. Zou, L. Yu, X. Fang, Y. Zheng, Y. Yang and C. Wang, *J. Pept. Sci.*, 2020, **26**, e3273.
57 Z. Khoshbin, M. R. Housaindokht, M. Izadyar, M. R. Bozorgmehr and A. Verdian, *Biotechnol. Bioeng.*, 2021, **118**, 555–578.
58 H. Meskher, T. Ragdi, A. K. Thakur, S. Ha, I. Khelfaoui, R. Sathyamurthy, S. W. Sharshir, A. K. Pandey, R. Saidur, P. Singh, F. Sharifian jazi and I. Lynch, *Crit. Rev. Anal. Chem.*, 2024, **54**, 2398–2421.
59 W. Li, Y. Gao, J. Zhang, X. Wang, F. Yin, Z. Li and M. Zhang, *Nanoscale Adv.*, 2020, **2**, 717–723.
60 A. Antonucci, J. Kupis-Rozmysłowicz and A. A. Boghossian, *ACS Appl. Mater. Interfaces*, 2017, **9**, 11321–11331.
61 A. Antonucci, J. Kupis-Rozmysłowicz and A. A. Boghossian, *ACS Appl. Mater. Interfaces*, 2017, **9**, 11321–11331.
62 L. Cai, W. Lv, H. Zhu and Q. Xu, *Phys. E*, 2016, **81**, 226–234.
63 J. Min, X. Rong, J. Zhang, R. Su, Y. Wang and W. Qi, *J. Chem. Theory Comput.*, 2024, **20**, 532–550.